Università degli Studi di Ferrara

DOTTORATO DI RICERCA IN FISICA

CICLO XXXIV

COORDINATRICE Prof. Luppi Eleonora

The SiPM Tracking Hodoscope for the JEDI Polarimeter

Settore Scientifico Disciplinare FIS/04

Dottorando:
Dott. Canale Nicola

Tutore
Prof Lenisa Paolo

Anni 2018 - 2022

A Noemi

Fatti non foste a viver come bruti,
ma per seguir virtute a canoscenza...

D. Alighieri

Contents

Introduction

One of the fundamental questions that humanity has grappled with is *Why do we exist?* Science is continually looking for answers to the concerns and problems relating to this fundamental question. Based on our current knowledge, it is unclear why there is more matter in our Universe than antimatter. The asymmetry of matter and antimatter can only arise if a set of parameters, known as the Sakharov conditions, are met. The violation of the $\mathcal{CP}$ symmetry is one of these criteria.

$\mathcal{CP}$ violation is included into the Standard Model of particle physics by CKM mechanism, but it is far from sufficient to explain the matter antimatter asymmetry of the Universe, so additional sources are required to fully comprehend it.

The Electric Dipole Moment (EDM) of fundamental particles is a very sensitive probe of further $\mathcal{CP}$ violation. Its discovery could enable the extension of the Standard Model and bring us closer to understanding this asymmetry. Despite the multiple searches for the EDM of different elementary particles, only the upper limits of EDM have been determined so far.

The Jülich Electric Dipole Moment Investigations (JEDI) collaboration is conducting one of these researches, with the goal of directly measuring the EDM of protons and deuterons in the accumulation ring [1].

While ultra-cold electrically neutral atoms and neutrons can conveniently be stored in traps, the measurement of an EDM of charged particles can only be approached with storage rings. EDM searches of charged fundamental particles have been impossible so far, due to the absence of the new class of electrostatic storage rings.

At this stage the JEDI collaboration works at the COoler SYnchrotron storage ring (COSY), to address the technical issues and feasibility studies at an existing facility, before venturing to the construction of dedicated electrostatic storage ring. COSY is a magnetic ring in which the beam is injected with vertical polarisation, then a spin-flipper changes it into horizontal plane. The existence of an EDM, combined with the presence of an electric field, would produce a torque on the spin of the particles, and thus a spin precession.

The measure of EDM is related to the time development of the beam polarisation, that is measured with a polarimeter that exploits the asymmetry of elastic scattering of charged particles off a carbon target. The JEDI POlarimeter (JEPO) is a modular calorimeter made of LYSO scintillating crystals coupled with SiPMs. The LYSO modules have a very high precision when it comes to calorimetry, but due to the limitations on its size the accuracy of particle trajectory reconstruction is compromised.

This thesis focuses on a possible upgrade for the existing JEPO: *i.e.* is the installation of a tracking hodoscope made of triangular plastic scintillator bars (the SiPM Tracking Hodoscope - SiTH). Due to the unique geometry of the arrangement and the individual readout of the tracker bars, this hodoscope will be capable of precisely determining the point of incidence of a particle on the polarimeter modules, thus increasing its performance in measurement of beam polarisation.

In 2018 a Test Beam was conducted on a prototype setup to find the performances of the SiTH modules. Based on the analysis of the data from 2018 Test Beam a Geant4 simulations of the SiTH detector has been performed. First of all the simulation aimed to match the 2018 Test Beam configuration to get the same result, then to exploit the energy resolution parameters in the simulation of the whole detector. Fig. 1 depicts the scheme of this approach to the simulations.

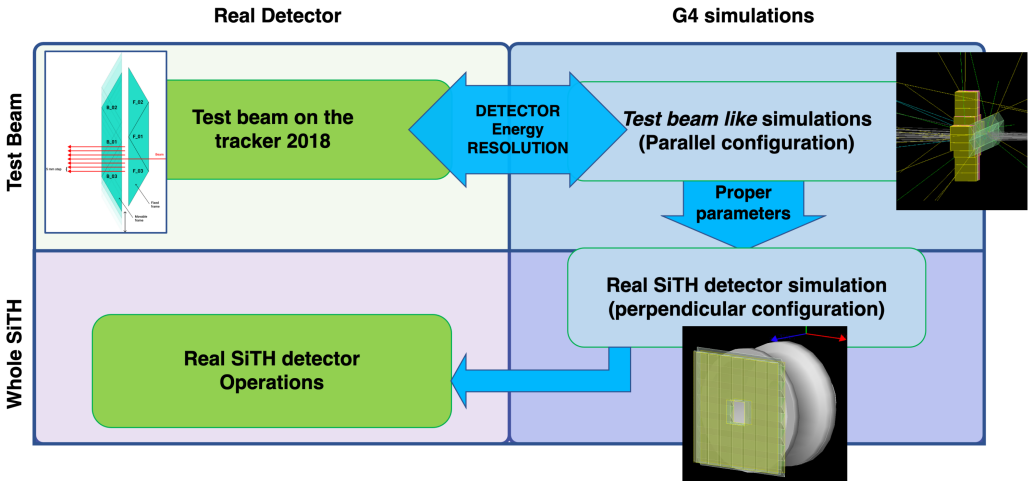

Figure 1: Simulations approach scheme. Starting from the Test Beam (top-left corner) the Geant4 simulation aims to find the proper *Detector Energy Resolution* parameter to exploit it in simulation of the whole SiTH detector (bottom-right corner), and then infer the real detector performance.

The following are brief overviews of the chapters to come:

- **Chapter 1**: This chapter discusses the scientific interest and motivation of EDM searches.
- **Chapter 2**: This chapter presents the ***Co****oler* ***Sy****nchrotron* (**COSY**) accelerator facility and the principle of Polarisation.
- **Chapter 3**: This chapter treats the concept, design and results of the **JE**DI **PO**larimeter.
- **Chapter 4**: This chapter illustrates the ***Si****PM* ***T****racking* ***H****odoscope* (SiTH) detector.
- **Chapter 5**: This chapter gives a summary of the results and an outlook for future operations.

Chapter 1

Scientific Motivation

This chapter briefly describes the open problem of matter-antimatter asymmetry and presents in detail the symmetries and transformations in particle physics.

Electric Dipole Moments (EDMs) of fundamental particle are presented, and an overview of the existing EDM experiments and their results is given.

The second part of the chapter addresses another open mystery of physics: *What is the universe made of*? Since, as inferred from cosmological observations, visible matter accounts only for a small fraction of the total observed one, the concept of Dark Matter has been introduced. Particles Beyond the Standard Model (BSM) have been proposed as Dark Matter candidates. These include ultralight particles like *axions* and *axion-like* particles (ALPs). Axions interact with gluons to produce an oscillating electric dipole moment (oEDM) on nucleons or nuclei.

1.1 Matter-Antimatter asymmetry

One of the biggest open questions of physics is the matter-antimatter asymmetry, because following the most commonly known models, matter and antimatter should be created in the same quantity. The universe after the Big Bang expanded exponentially, in a process called inflation. After the inflation stopped the temperature was still high enough to create, and so annihilate, particle-antiparticle pairs in thermal equilibrium. Then, when the

universe cooled down enough to reach the critical energy for pair production, this pair production was no longer accessible and so, matter and antimatter could annihilate into photons [2]. A schematic view of the universe expansion is shown in Fig. 1.1.

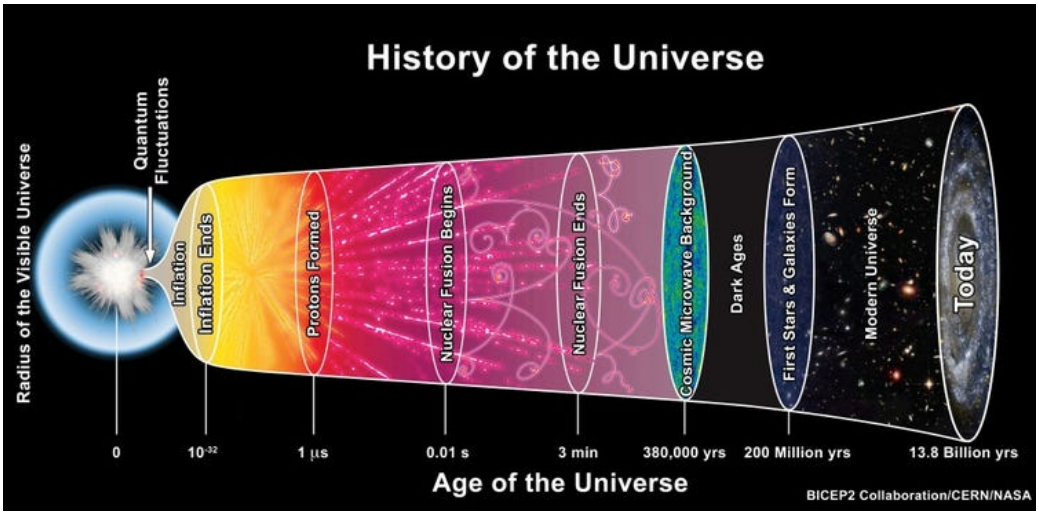

Figure 1.1: Universe expansion scheme. During the Big Bang the matter and antimatter were formed in equivalent amount, in a successive phase baryons and anti-baryons formed and annihilated into photons. 380.000 years after Big Bang the universe time became transparent to the photons, and these photons are red-shifted to microwave frequencies due to the expansion of the universe.

A sturdy quantity to express this asymmetry is the so-called baryon asymmetry:

$$\eta_{B\overline{B}} = \frac{N_B - N_{\overline{B}}}{N_\gamma}. \tag{1.1}$$

Which is the difference of the baryon (N_B) and anti-baryon ($N_{\overline{B}}$) densities over the cosmic background radiation photon density (N_γ) just before the disappearance of the anti-baryons [3]. The $\eta_{B\overline{B}}$ is part of cosmological models and experimentally determined using astrophysical observation. An experimental evidence to determine $\eta_{B\overline{B}}$ is the abundance of light elements produced during Big Bang Nucleosynthesis (BBN). Another evidence is the observed temperature fluctuation in the Cosmic Microwave Background (CMB) within the Wilkinson Microwave Anisotropy Probe (WMAP) experiment. Both results were in good agreement in the baryon asymmetry measurement

stated in [2]:

$$\eta_{B\overline{B}}^{CMB} = 6.16^{+0.153}_{-0.156} \cdot 10^{-10}. \tag{1.2}$$

$$\eta_{B\overline{B}}^{BBN} = 6.07^{+0.33}_{-0.33} \cdot 10^{-10}. \tag{1.3}$$

However, the estimation based on the Standard Model of particle physics (SM) and Standard Model of Cosmology (SMC) yield an $\eta_{B\overline{B}} \approx 10^{-18}$, which is eight orders of magnitude below the measured values [4].

The absence of the antimatter can have two possible explanations. One is that the antimatter still exists in regions separated from matter-dominated areas. So the Milky Way (*e.g.*) is part of such a matter-dominated region as a result of an observation of the matter excess. The other is that the antimatter annihilation was an asymmetrical process during the baryogenesis. The first case implies the search for antimatter, as done by Alpha Magnetic Spectrometer (AMS) experiment on the International Space Station (ISS) [5].

For the baryogenesis Andrei Sakharov in 1967 postulated three conditions to be fulfilled [6]:

- **Baryon number violation:** Considering that the baryon number B was initially zero, the baryon number violation is necessary to reach a state where there is an excess of matter over antimatter.
- **Violation of $\mathcal{C}$ and $\mathcal{CP}$ symmetries:** The probability of particle or antiparticle creation only differs if the symmetries of charge conjugation $\mathcal{C}$ and the combined charged and parity transformation $\mathcal{CP}$ are violated.
- **Being out of thermal equilibrium:** When a system is in thermal equilibrium the likelihood of processes that take place are just as much as the reversed ones. Therefore, the system would be unable to transit from a $B = 0$ to a $B \neq 0$ state.

The $\mathcal{CP}$ violation incorporated in the SM is not enough to explain the measured $B\overline{B}$ asymmetry. Permanent EDMs of the elementary particles are candidates for such processes which will be discussed later in this chapter.

1.2 Symmetries and Transformations

A symmetry, in general, is an operation that maintains the invariance of a system. Noether's theorem on the connection between conservation principles and symmetries makes symmetries significant tools in elementary particle physics. A conservation law is connected to each continuous symmetry in nature. Each conservation law, in other words, represents an underlying symmetry. The universe's time and space translation symmetries, for example, result in energy and momentum conservation, and angular momentum conservation is linked to a physical system's rotational symmetry [7].

Parity Transformation

Parity operator $\mathcal{P}$ is also called *space inversion* operator. In fact using $\mathcal{P}$ is the same as reversing all three spatial coordinates while keeping the temporal coordinates.

$$(\vec{x}, t) \rightarrow (\vec{x}^{\,\prime}, t^{\,\prime}) = (-\vec{x}, t). \tag{1.4}$$

As a result, being symmetric under the parity transformation indicates that a process and its mirror image process behave identically. The transformation affects polar vectors like displacement, momentum, and acceleration, but not axial vectors as angular momentum. In an electromagnetic physical system, electric fields represented by polar vectors will be reversed by the $\mathcal{P}$ transformation, but magnetic fields will maintain their orientation since they are axial vectors.

The electromagnetic and strong interactions of the SM are symmetrical under $\mathcal{P}$, while the weak interaction violates it. Following the finding of K^+ meson decaying into two and three pions, respectively, Lee and Yang proposed in 1956 to explore parity violation for weak interactions by exploring β decays [8]. Soon after, Wu et al. carried out an experiment about the beta decay of polarized ^{60}Co [9]:

$$^{60}Co \rightarrow ^{60}\ Ni + e^{-} + \overline{\nu}_e. \tag{1.5}$$

It was discovered that no matter what the sign of the magnetic field was, the emitted electrons were more likely to fly in the opposite direction of

the nuclear spin. Since the parity operator has no effect on the polarisation direction but influences the momentum and hence the flight direction under $\mathcal{P}$, the measurement provides evidence of parity violation. Furthermore, research into charged pion decays revealed that the neutrino spin is always anti-aligned to the momentum vector, but the spin of the anti-neutrino points along the path of flight. Consequently, assuming mass-less neutrinos, just left-handed neutrinos and right-handed anti-neutrinos couple to the weak interaction in the SM [10].

Charge Conjugation Transformation

The charge conjugation Operator $\mathcal{C}$ replaces particles with their antiparticle in the underlying physical processes. As a result, additive quantum numbers like charge, baryon, and lepton number, as well as strangeness, are reversed, but spin, position, and momentum are unaffected. Inverting the charge causes the electric and magnetic fields to shift direction. The weak component of the SM contains violations of the $\mathcal{C}$ symmetry. Consider the $\mathcal{C}$ transformation of a left-handed neutrino into a left-handed anti-neutrino to find proof for a $\mathcal{C}$ violation. Left-handed anti-neutrinos do not join in weak interactions in the SM, as previously stated. [11, 12].

Time Reversal Transformation

Time reversal $\mathcal{T}$ is the third discrete transformation. It inverts the sign of the time coordinate while keeping the spatial coordinates unaltered.

$$(\vec{x}, t) \rightarrow (\vec{x}^{\,\prime}, t^{\,\prime}) = (\vec{x}, -t). \tag{1.6}$$

The specific reaction rate for a time symmetric process should be the same as for the reverse reaction. There is no evidence for $\mathcal{T}$ violation in several experiments regarding strong and electromagnetic interactions. Experiments in the weak sector are difficult to carry out, however by using the $\mathcal{CPT}$ theorem, a reliable measurement for $\mathcal{T}$ violation in weak interactions may be carried out. For Lorentz invariant local quantum field theory, the $\mathcal{CPT}$ theorem asserts that each combination of all transformations ($\mathcal{CPT}$) results in a symmetric process [13]. As a result, a ($\mathcal{T}$) violating process is also a ($\mathcal{CP}$)

violator. The rate asymmetries that emerged from measuring the probability of the transformation $\overline{K}^0 \to K^0$ and the reversed process $K^0 \to \overline{K}^0$ proved a direct violation of the ($\mathcal{T}$) symmetry [14]:

$$\left\langle \frac{R(\overline{K}^0 \to K^0) - R(K^0 \to \overline{K}^0)}{R(\overline{K}^0 \to K^0) + R(K^0 \to \overline{K}^0)} \right\rangle = (6.66 \pm 1.3_{stat} \pm 1.0_{sys}) \cdot 10^{-3}. \quad (1.7)$$

$\mathcal{CP}$ Violation in the Standard Model

After the evidence of parity violation in the weak sector of the SM, the $\mathcal{CP}$ symmetry was designed to explain the observed left-right symmetry in nature. In the $\mathcal{CP}$ transformation a parity transformation is applied first, followed by a charge conjugation. The meson decay problem can be solved by combining these two processes. A left-handed neutrino is transformed into a right-handed anti-neutrino through the $\mathcal{CP}$ transformation [11, 13]. In the Fitch-Cronin experiment of 1964, which studied the decay of the K^0 particle, a violation of $\mathcal{CP}$ symmetry in weak interactions was discovered [15]. The decay rates of kaons to two and three pions for the mass eigenstate K_L were measured. The decay into two pions would be impossible if K_L were a pure $\mathcal{CP}$ eigenstate. Furthermore, across the experiment, several of these decays were recorded, indicating $\mathcal{CP}$ violation in the weak sector. The Cabibbo-Kobayashi-Maskawa (CKM) matrix might well be incorporated to the SM to explain this phenomenon. CKM matrix describes the quarks mixing, whose empirical phase δ is related to $\mathcal{CP}$ violation. The SM, in general, admits $\mathcal{CP}$ violation in strong interactions.

The so-called θ-QCD term in the QCD Lagrangian violates $\mathcal{CP}$, but no comparable processes have been seen in the strong sector, leading to the so-called strong $\mathcal{CP}$ issue [16]. Additional sources of $\mathcal{CP}$ violation are of significant interest because the $\mathcal{CP}$ violation in the CKM matrix is not capable of explaining the matter-antimatter imbalance. One such possibility is the EDM, which will be examined in the following sections.

1.3 Electric Dipole Moments

The EDM, like momentum, charge, spin and mass, is a fundamental property of a particle. The presence of a permanent EDM in a non-degenerated system might be another probe of $\mathcal{CP}$ violation, and it would explain matter predominance across the universe. The basic concept of EDMs is briefly discussed in this section, as well as an overview of EDM measurements and their conclusions.

1.3.1 Definition

Generally EDM d is defined as the separation of positive and negative charges in a system. EDM is a vector quantity consisting of two charges q and $-q$ separated by a distance r.

The EDM of a basic particle can be defined as follows in the context of quantum mechanics:

$$\vec{d} = d \cdot \vec{s} \text{ with } d = \eta_{EDM} \frac{q\hbar}{2mc}, \tag{1.8}$$

where the q is the charge of the particle and m its mass and $\hbar$ is the reduced h Plank constants. The η_{EDM} is a dimensionless quantity.

Eq. 1.8 has a similar structure to the magnetic dipole moment (MDM) one:

$$\vec{\mu} = \mu \cdot \vec{s} \text{ with } \mu = g \frac{q\hbar}{2m}. \tag{1.9}$$

Here q is the charge of the particle and m its mass. The so-called g-factor, g, is dimensionless,. The MDM must be aligned with the spin s to maintain its vector character, as this is the only quantization axis available.

The presence of EDM would violate the $\mathcal{P}$ and the $\mathcal{T}$ invariances and so the $\mathcal{CP}$, as mentioned before. This may be observed by applying the $\mathcal{P}$ and $\mathcal{T}$ transformations to the Hamiltonian that describes the EDM and MDM in external electric E and magnetic B fields for a particle at rest (see section 1.2 for symmetries reference):

$$\hat{H} = -\vec{\mu} \cdot \vec{B} - \vec{d} \cdot \vec{E} \tag{1.10}$$

$$\mathcal{P}: \hat{H} = -\vec{\mu} \cdot \vec{B} + \vec{d} \cdot \vec{E} \tag{1.11}$$

$$\mathcal{T}: \hat{H} = -\vec{\mu} \cdot \vec{B} + \vec{d} \cdot \vec{E}. \tag{1.12}$$

Equation 1.11 uses a parity transformation to flip the direction of the electric field $\vec{E}$ while leaving the magnetic field $\vec{B}$ and the spin $\vec{s}$ intact. The EDM term's sign shifts, while the MDM term stays the same. As a result, the EDM breaks the $\mathcal{P}$ invariance, but the MDM retains the parity. The time reversal transformation of Equation 1.12, in which the spin and magnetic fields are flipped but the electric field stays unchanged, is the same. This means that, since EDM points in the spin direction, the EDM term of the equation 1.10 $\mathcal{T}$ violates changing the sign.

Figure 1.2 illustrates the aspects discussed above. According to the $\mathcal{CPT}$ theorem, an EDM is $\mathcal{CP}$ violating since it violates individually both $\mathcal{P}$ and $\mathcal{T}$.

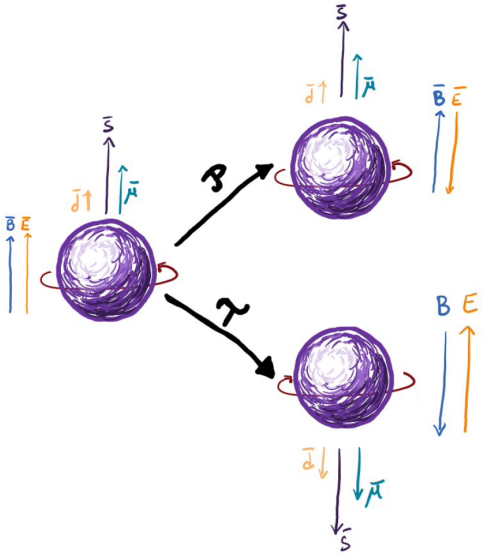

Figure 1.2: A particle in an external magnetic B and electric E field, with a persistent EDM, is represented schematically in this diagram. The electric field changes sign but the magnetic field and spin remain constant in a parity transformation $\mathcal{P}$. The time reversal transformation $\mathcal{T}$, on the other hand, reverses the MDM and the EDM, and also changes the sign of the magnetic field. As a result, a system with a permanent EDM breaks both symmetries, and is also $\mathcal{CP}$ violating, according to the $\mathcal{CPT}$ theorem.

1.3.2 $\mathcal{CP}$ violation and EDMs

EDMs can be introduced via higher order loop effects for both weak and strong sections of the SM. The following is a short review of the relevant mechanism and the SM prediction that results.

The imaginary phase δ of the CKM matrix, as indicated in Section 1.2, contributes to $\mathcal{CP}$ violation in the weak sector of the SM.The predicted values of EDM for neutrons and electrons are the following:

$$d_n \approx 10^{-32}\, e \cdot \mathrm{cm} \tag{1.13}$$

$$d_e \approx 10^{-40}\, e \cdot \mathrm{cm} \tag{1.14}$$

Because the major contribution to proton and neutron EDMs is at the three-loop level, these quantities turn out to be extremely tiny. The EDM is even produced on the four-loop level in the case of the electron [17].

1.3.3 Existing EDM measurement

Since the EDM is a potential probe of the new $\mathcal{CP}$ violation, several tests have been conducted looking at different particles. The polarisation of a particle ensemble turns out to be the most relevant observable for EDM experiments since the EDM affects the spin motion (see equation 1.8). The next paragraphs describe the fundamental concept of these measurements for the neutral systems. With in presence of electromagnetic fields, the polarisation variation for trapped particles is studied. A particle sample with polarisation parallel to a main magnetic field is required at first, and the spins begin to precess with an initial Larmor frequency. The precession frequency is put in resonance with an RF field as the system absorbs it making it measurable. An uniform electric field is applied in the third stage and interacts with the particles' EDMs. Both the MDM and the EDM lead to a shift in the precession frequency of the spins. The polarity of the electric field is flipped inside the experiment to obtain pure EDM contribution as shown in Fig. 1.3.

The difference in Larmor precession frequencies $\Delta\omega$ as a result of the two parities is proportional to the EDM and may be written as:

$$\Delta\omega = \omega(E\uparrow) - \omega(E\downarrow) = \frac{4|\vec{d}|E}{\hbar}, \tag{1.15}$$

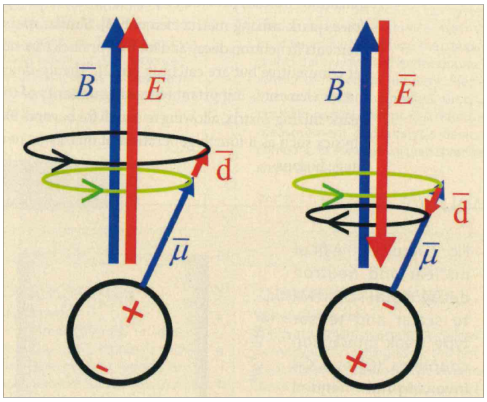

Figure 1.3: A non zero permanent EDM, **d**, would mean that the time-averaged position of positive and negative charges inside the particle would not coincide. The presence of an EDM would cause a precession of the spin when placed in an electric field **E** (in black). The magnetic moment μ, that does not violate $\mathcal{CP}$ symmetry, causes a spin precession in a magnetic field **B** (in green). A non-zero EDM would cause a difference in the precession frequency when placed in an alternately parallel (left) and antiparallel (right) magnetic and electric fields [18].

The arrows represent the different polarities of the electric field, while $\hbar$ stands for the reduced Planck constant. After the interaction with the electric field, it is measured by adding another RF magnetic field. The resultant vertical polarisation is used to calculate the frequency difference in Equation 1.15 and acts as a measure for the EDM.

First measurement of neutron's EDM was provided by Smith, Ramsey and Purcell in 1957 [19], with a result of :

$$d_n = (0.1 \pm 2.4) \cdot 10^{-20}\, e \cdot \text{cm}. \tag{1.16}$$

There are numerous physics theories BSM that incorporate EDMs and may thus predict the EDMs of various particles. It is important to measure the EDM not just for neutrons but also for a variety of other particles in order to explore these hypotheses and compare predictions to experimental evidence. Because the EDM values are extremely small and can easily be dominated by systematic errors, it is critical for the experiments to achieve very high sensitivity in this setting. Because the results are in agreement with zero, all previous measurements have only provided upper limits for the EDMs.

Table 1.1 and Figure 1.4 summarize the upper bounds for the EDM of the most investigated particles. It's worth to mention that the proton and

electron boundaries are determined by indirect measurements of atoms and molecules. As a consequence, assumptions regarding how nuclei behave in these systems have a role in determining these numbers [20]. The muon EDM, on the other hand, was generated from a direct measurement utilizing μ^+ and μ^- beams at the Brookhaven National Laboratory's $g-2$ experiment (BNL). It's the only direct EDM experiment that uses charged particles so far. Heavy nuclei, such as deuterons, will be the subject of further studies in the near future [21, 22].

Particle	upper EDM limit ($e \cdot$ cm)	C.L.
neutron	$d_n \leq 1.8 \cdot 10^{-26}$	90%
proton	$d_p \leq 7.9 \cdot 10^{-25}$	90%
electron	$d_e \leq 8.7 \cdot 10^{-29}$	95%
muon	$d_\mu \leq 1.9 \cdot 10^{-19}$	95%

Table 1.1: Table with measured upper limits for fundamental particles [23–26]

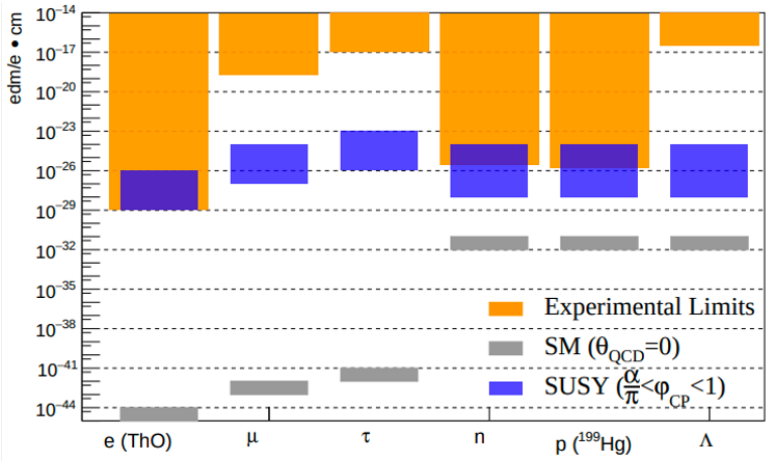

Figure 1.4: Graphical representation of measured upper limits for different particles EDMs [27].

1.3.4 EDM Searches in Storage Ring

When particles are charged, trapping and studying them under the influence of electromagnetic fields becomes much more difficult. In the presence of electric fields, charged particles accelerate and cannot be trapped as easily

as neutral particles like neutrons. As a result, new measuring methods must be implemented [28]. Storage rings provide the advantage of storing charged particles and cycling them for extremely extended beam lifetimes.

The essential idea for a storage ring-based EDM search is the same as it is for neutral systems, except that the particle is trapped in a larger region [29]. The storage ring serves as a charged particle trap. The time evolution of the Polarisation of the stored particle is then analysed. An electric field is supplied, similar to the neutral systems, with which the EDM of the particles interacts, changing the spin orientation of the particle and therefore the polarisation.

A vertically polarized particle beam is injected in the storage ring, that traps it by magnetic or electric fields. A Lorentz translation into the particle's rest frame yields the fields operating on the spin, which are a linear combination of the fields in the laboratory frame. A vertical oscillation of the polarisation is produced as a result of the EDM's interaction with the fields, with the frequency:

$$\vec{\omega}_{EDM} = -\frac{q}{mc}\frac{\eta_{EDM}}{2}(\vec{E} + c\vec{\beta} \times \vec{B}). \tag{1.17}$$

Moreover, due to the MDM the polarisation precesses in the horizontal direction, with a frequency of ω_{MDM}:

$$\vec{\omega}_{MDM} = -\frac{q}{m}\left[\left(G + \frac{1}{\gamma}\vec{B}\right) + \left(G + \frac{1}{1+\gamma}\right)\vec{\beta} \times \frac{\vec{E}}{c}\right], \tag{1.18}$$

where the fields $\vec{E}$ and $\vec{B}$, as well as the velocity $\vec{\beta}$, are all perpendicular to each other. The anomalous magnetic moment, which may be linked to the g-factor by $G = \frac{g-2}{2}$, is the factor G. One method to address the problem is to try to maintain the polarisation projection in the horizontal plane parallel to the momentum by matching the particle's revolution frequency to the MDM's precession. This is the *Frozen Spin* situation [28] in which the magnetic and electric fields must be matched in a certain way. This can be achieved in a variety of ways depending on the particle. In the presence of only electric fields and no magnetic fields particles with a positive G can have *Frozen Spin* at a specific momentum. A particle with negative G, on the other hand, always needs both electric and magnetic fields. If the *Frozen Spin* condition is fulfilled, the only term that contributes to the spin manip-

ulation is the EDM, which results in a vertical polarisation accumulation, a scheme of this principle is shown in Fig.1.5.

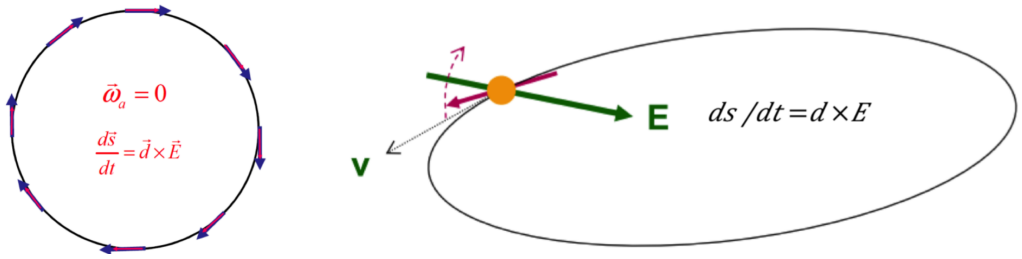

Figure 1.5: Principle of EDM search in a storage ring. A longitudinally polarized particle bunch, under *Frozen Spin* condition, will gradually build up vertical Polarisation in response to a radial electric field due to EDM. This can be measured by high precision polarimeters.

1.4 Axions and Dark Matter

Among the deepest mysteries in natural sciences stands the question of what the universe is made of. Visible matter, comprising Standard Model particles, accounts only for a small fraction. As inferred from cosmological observations, about 5 times more matter is invisible and is called Dark Matter (DM). Dark Matter has been postulated by the need for much more mass than actually seen in rotating galaxies in order to bind them by the gravitational force, compensating the centrifugal force. This is schematically shown in Fig. 1.6.

There are further compelling observations indicating the existence of DM, *e.g.* gravitational lensing and its role in the evolution of structure in the Universe. However, what DM actually is, remains a mystery. It is important to note that none of the known building blocks of the (otherwise remarkably successful) Standard Model (SM) of elementary particle physics can serve as DM. This implies that the SM of particle physics provides no solution to the DM problem. As a consequence new particles outside the realm of the SM (Beyond Stadard Model - BSM) have been proposed as dark matter candidates . Among them are so called WIMP (Weakly Interacting Massive Particles). In spite of enormous experimental effort, no DMparticle was found up to now. It it thus important to widen the search to other, theoret-

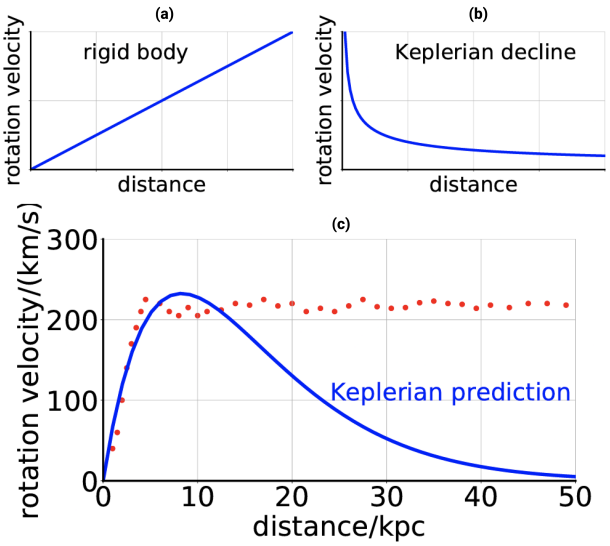

Figure 1.6: Rotational speed for a rigid body (**a**) and for Keplerian motion, *e.g.* our solar system, with most of the mass centered at zero (**b**). In **c** the result (red dots) for a typical spiral galaxy is shown. The disagreement with the Keplerian prediction for R $>$ 10 kpc (*i.e.* the constant speed) was first observed by F. Zwicky in the 1930s in the Coma Cluster and indicates that more mass than visible must be present. [30]

ically well motivated DM candidates [31]. These include ultralight particles like axions and axion-like particles (ALPs).

Originally, axions were suggested to address the so-called strong $\mathcal{CP}$-problem in particle physics' Standard Model. θ_{QCD} term of the Lagrangian of the QCD contributes to $\mathcal{CP}$ violation in the strong sector of the SM is:

$$\mathcal{L}_\theta = -\theta_{QCD}\frac{g_s^2}{64\pi^2}\epsilon^{\mu\nu\alpha\beta}G^\alpha_{\mu\nu}G^\alpha_{\alpha\beta}, \tag{1.19}$$

where g_s is the strong coupling constant, $G^\alpha_{\mu\nu}$ the gluon field tensor and ϵ describes the 4D Levi-Civita tensor. The θ_{QCD} factor can contribute to higher EDM values if compared to the influence of the weak sector.

The predictions for the neutron and proton are as follows [32]:

$$d_n \approx \theta_{QCD}\,(-2.9 \pm 0.9)\cdot 10^{-16}\, e\cdot\text{cm} \tag{1.20}$$

$$d_p \approx \theta_{QCD}\,(1.1 \pm 1.1)\cdot 10^{-16}\, e\cdot\text{cm} \tag{1.21}$$

In general, θ_{QCD} can take on any value, but neutron EDM observations provide an upper limit of [33]:

$$\theta_{QCD} < 10^{-10}. \tag{1.22}$$

θ_{QCD}'s smallness is referred to as the strong $\mathcal{CP}$ issue since it is theoretically unexplained. The inclusion of a new symmetry naturally explains the smallness and results in the creation of a new particle, the *axion* [34, 35]. If axions are the source of dark matter, they must be exceedingly light, with masses less than 10^{-6}eV, about 12 orders of magnitude lighter than the electron.

Axions potentially interact with regular matter in a number of different ways. The axion-photon interaction is at the heart of the majority of axion searches. Other investigations involve the usage of axion interactions with atomic nuclei or spin coupling. The well-known nuclear magnetic resonance method [36] can be employed to investigate the latter effects.

1.5 Axion searches in Storage Ring and oEDMs

The influence of axions on the spin motion of a particle ensemble in a storage ring will be investigated [37]. Axions interact with gluons to produce an oscillating electric dipole moment (oEDM) on nucleons or nuclei [38]. These oEDMs may be detected in a storage ring using resonant techniques, which magnify the effects and allow for remarkable precision.

The experimental approach is depicted in Fig.1.7. Spin polarized particles are kept in a storage ring as a beam in a circular orbit. The polarisation vector P, which is determined by the average of the spin vectors S in a particle cluster, precesses with a frequency Ω_{MDM} due to the MDM. If the axion oscillation frequency, ω_{axion}, matches the Ω_{MDM}, a resonance occurs, and a vertical polarisation build-up owing to the oEDM is seen.

The precession frequency Ω_{MDM} in a magnetic storage ring such as COSY is determined by the particle's energy and the magnetic moment:

$$\Omega_{MDM} = \gamma\, G\Omega_{rev}, \tag{1.23}$$

where γ stands for the relativistic Lorentz factor, G for the magnetic anomaly and Ω_{rev} is the angular revolution frequency of the beam. When an electric

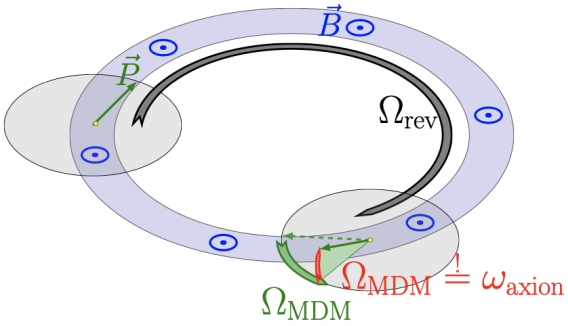

Figure 1.7: Polarisation $\vec{P}$ has a precession in horizontal plane with angular frequency Ω_{MDM}. If $\Omega_{MDM} = \omega_{axion}$ a resonant build-up of vertical polarisation may be seen thanks to the oEDM [30].

or a magnetic field is applied to a particle the spin vector $\vec{S}$ precesses due to $\vec{d}$ or $\vec{\mu}$ and has to be aligned with the spin direction. Looking at this spin precession one can access the MDM and EDM of the particle. Axions and axion-like particles (ALP) could induce an oscillation in the EDM, of the nuclei with a frequency given by the Compton frequency ω_{axion}:

$$\omega_{axion} = \frac{m_a c^2}{\hbar}, \tag{1.24}$$

with axion mass written as m_a. Using resonance effects, the oscillation of the EDM $\vec{d}$ can be investigated in storage rings.

This principle is quite similar to the one described in EDM searches in storage ring in section 1.3.4 and this make the COSY facility an available host for experiments that search for axions and oEDMs for protons and deuterons [30]. When compared to other studies seeking axion generation or absorption, axion searches at storage rings have the benefit of being able to cover a wide mass (frequency) area (with reduced sensitivity to the axion-gluon interaction) or concentrate on a very limited mass region (with a much higher sensitivity). The second situation is interesting if another experiment provides evidence for an axion or ALP at a particular mass. In this instance, the available measuring time would be spent on a precisely single frequency, matching to the mass m_a, and looking for a resonance signal, so verifying any claim (see. Fig.1.8 for the sensitivity spectra).

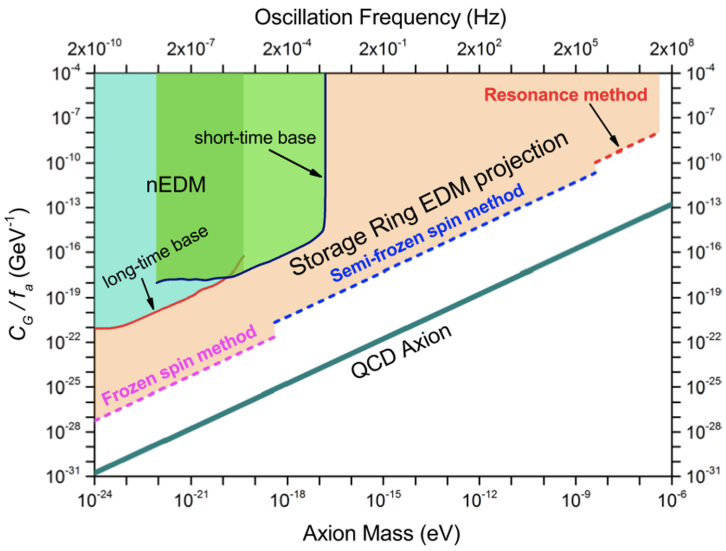

Figure 1.8: One Year data acquisition sensitivity of the axion-gluon coupling over Axion mass (eV) or frequency (Hz)

Chapter 2

The Cooler Synchrotron COSY

In this chapter the ***Co****oler* ***Sy****nchrotron* (**COSY**) accelerator facility is described. A brief overview of the facility's main components and experimental halls is given.

JEDI collaboration aims to directly measure the EDM of protons and deuterons in the accumulation ring. The combination of EDM with the presence of an electric field, would produce a torque on the particle, and thus a spin precession. Therefore, to achieve the primary goal of JEDI, the experiment needs to look at the time development of the polarisation of the particle beam.

The formal definition of polarization is given in this chapter.

2.1 General Overview

COSY accelerator facility is located at *Forschungszentrum Jülich* in Germany. A scheme of COSY is given in Fig.2.1.

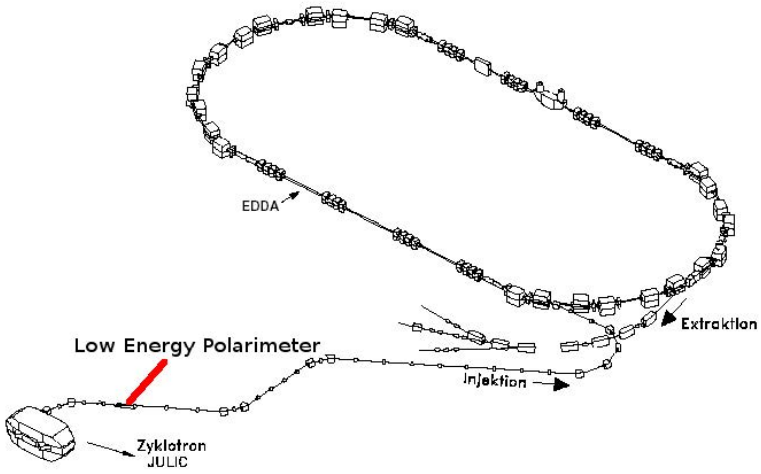

Figure 2.1: COSY schematic view

The accelerator consists in a storage ring of 184 m circumference, which can accelerate and store beams of polarised or unpolarised protons and deuterons up to 3.7 GeV/c. The facility counts three main parts: A source that produces polarised and unpolarised beams (hydrogen H^- and deuterium D^-). This source beam are transferred into the injection cyclotron JULIC (***Jül****ich* ***I****sochronous* ***C****yclotron*). The JULIC accelerates the kinetic energy of ion beams up to 45 MeV for H^- beams and up to 76 MeV for D^- beams target. From there the beams are moved via an injection beam line, where a small polarimeter (the ***L****ow* ***E****nergy* ***P****olarimeter* (LEP)) is installed, this polarimeter can measure the polarisation of the injected beam using elastic scattering on a thin carbon foil target. COSY can reach momenta up to 3.7/c GeV which equals kinetic energies of $\sim$ 2.8 GeV in case of protons and $\sim$ 2.2 GeV for deuterons [39]. The COSY accelerator is composed by two straight sections of 40 m located in between two semi-circular ones of radius 16.5 m [40]. The dipoles that keep the beam in orbit are normal-conducting water cooled magnets, that can reach magnetic fields up to 1.58 T. Beam optics is composed by groups of quadrupole magnets in a row. The real acceleration occurs in the radio-frequency (RF) cavity that is located in the middle of one of the straight sections. If a beam of electrons with same velocity of the main beam is injected in a short section of the ring, the electrons can scatter elastically with the beam particles and reduce the

transversal momentum component of their scattering partner. The electrons can be scattered out of the beam or be removed by the electron cooler once they reach the end of this section. The stochastic cooler allows the sampling of the beam position with a very fine subdivision of bunches as they enter through the so-called *pick-up detector*. For each bunch entering the detector, deviation from the ideal orbit is obtained. This measurement is transferred to a device called *The Kicker* with a wave-guide diagonally across the ring. The particle bunch needs to travel through all of the beam pipe, and once it enters the kicker, a correction signal, proportional to the measured deviation, is applied at the pick-up. This method allows for the reduction of the phase space, both for longitudinal as well as for the transverse direction of the beam.

The straight sections allow COSY to host up to two experiments in the ring. The WASA detector and the JEPO detector are installed in these straight sections. In WASA, the target produces elastic scattering reactions and can be moved into the beam pipe in front of the detector. The beam orbit can be set such that it will pass just below the target during the acceleration time. When it reaches the final energy the excited beam is broadened, so a small fraction of it hits the target and scatters into the detector. Feedback loop between the detector rate and the excitation assures that the full beam is extracted on the target.

COSY can extract the accelerated beam using a magnetic septum and so, transfer it via the extraction beam line to the external experiment hall (former *Big Karl* experimental hall).

2.2 Polarisation

As previously stated the primary goal of this project is to analyse the time development of the polarisation of a particle beam, so a formal definition of polarisation is critical. The spin of elementary particles like quarks or electrons, but also composite particles like neutrons, protons, or even nuclei, may be represented as intrinsic angular momenta, and are expressed in (full-or-half-integer) multiples of the reduced Planck constant $\hbar$. *Fermions* are particles having a half-integer spin. As a result, fermions include all quarks and leptons. *Bosons* are particles having an integer spin. The spin is the sin-

gle quantization axis in a quantum system, which means that other vectorial characteristics, such as the magnetic moment or the electric dipole moment, must be aligned with this axis. The quantum number s determines the spin itself. $s = \frac{1}{2}$ for a proton, which is a fermion, and $s = 1$ for a deuteron, which is made up of a proton and a neutron and therefore is a boson. The spin can be configured in several ways in connection to its quantization axis, which is referred as the z-axis by convention. $(2s + 1)$ different configurations can be discovered for a particle with a spin of s. The quantum number m, which can have values in the range $[s, s - 1, ..., -s + 1, -s]$, denotes these configurations. Figure 2.2 shows a schematic representation of these configurations for a spin-1/2 and spin-1 particle.

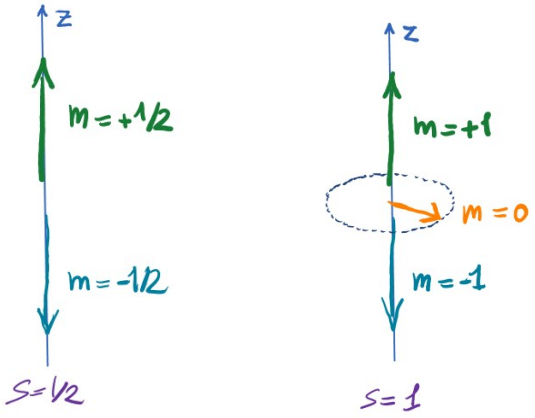

(a) Spin$-\frac{1}{2}$ configuration.

(b) Spin-1 configuration.

Figure 2.2: Spin configuration for spin-$\frac{1}{2}$ particles (*e.g.* the proton) and spin-1 particles (*e.g.* the deuteron)

It's pointless to talk about spin in a beam of one species of particles because it's a property of the individual particle. Rather, a statistical indicator related to the likelihood of detecting a particle with a specific spin configuration in the beam is required. Polarisation is the name for this beam characteristic, which can be defined as follows: Consider a beam of spin$-\frac{1}{2}$ particles with $N^{\uparrow}$ particles in the $m = +\frac{1}{2}$ configuration and $N^{\downarrow}$ particles in the $m = \frac{1}{2}$ configuration. The following is how vector polarisation is defined:

$$P_y = \frac{N^{\uparrow} - N^{\downarrow}}{N^{\uparrow} + N^{\downarrow}} = p^{\uparrow} - p^{\downarrow}, \tag{2.1}$$

The probabilities of finding a particle with $m = +\frac{1}{2}$ and $m = -\frac{1}{2}$ are denoted by $p^{\uparrow}$ and $p^{\downarrow}$, respectively. The vector polarisation for a beam of spin $-\frac{1}{2}$ particles can be as follows:

$$-1 \leq P_y \leq +1, \tag{2.2}$$

this indicates that vector polarisation values can range from -100% to 100%. For spin-1 particles, the beam can be made up of $N^{\uparrow}$ particles in the $m = +1$ configuration, $N^{\downarrow}$ particles in the $m = -1$ configuration, and N^0 particles in the $m = 0$ configuration. The vector polarisation is defined similarly to the spin $\frac{1}{2}$ particles:

$$P_y = \frac{N^{\uparrow} - N^{\downarrow}}{N^{\uparrow} + N^{\downarrow} + N^0} = p^{\uparrow} - p^{\downarrow}, \tag{2.3}$$

Because the spin-1 particles have three different configurations, an extra polarisation, the tensor polarisation, must be defined:

$$aP_{yy} = \frac{N^{\uparrow} - 2N^0 + N^{\downarrow}}{N^{\uparrow} + N^{\downarrow} + N^0} = p^{\uparrow} - 2p^0 + p^{\downarrow} = 1 - 3p^0, \tag{2.4}$$

The vector polarisation can be the same as for spin$-\frac{1}{2}$ particles, however the tensor polarisation can be any of the following:

$$-2 \leq P_{yy} \leq +1. \tag{2.5}$$

The vector and tensor polarisation for spin-1 particles are linked according to their definition. As a consequence, the vector polarisation values in a beam with no tensor polarisation are limited to the following:

$$P_{yy} = 0 \rightarrow -\frac{2}{3} \leq P_y \leq +\frac{2}{3} \tag{2.6}$$

Setting $P_{yy} = 0$ in Equation 2.4 results in $p^0 = \frac{1}{3}$ as in the expression above.

2.3 Polarised Source

The polarised particle source is a colliding beam source [41]. The layout of the source is shown in Fig. 2.3. The basic idea is to start with an electrically

neutral, polarised beam of hydrogen or deuterium atoms. When this atomic beam collides with an atomic caesium beam, one electron from a caesium atom is transferred to the polarised atom. The nucleus' polarisation is maintained in the generated negative ion. The negative ions can then be extracted and accelerated before being introduced into COSY in the cyclotron.

The hydrogen or deuterium molecules in the atomic beam source, are first split into single ones using an electric discharge. To decrease recombination, small quantities of oxygen and nitrogen are introduced. The atoms are cooled to around 30 K after passing through a nozzle.

The magnetic moment of their electron and hyperfine coupling are used to polarize the dissociated atoms. The electron angular momentum L (0 in the ground state) and spin S combine to form the total spin J. This spin couples with the nuclear spin I to form a total spin F in a weak magnetic field, small in comparison to a particular value B_{crit}.

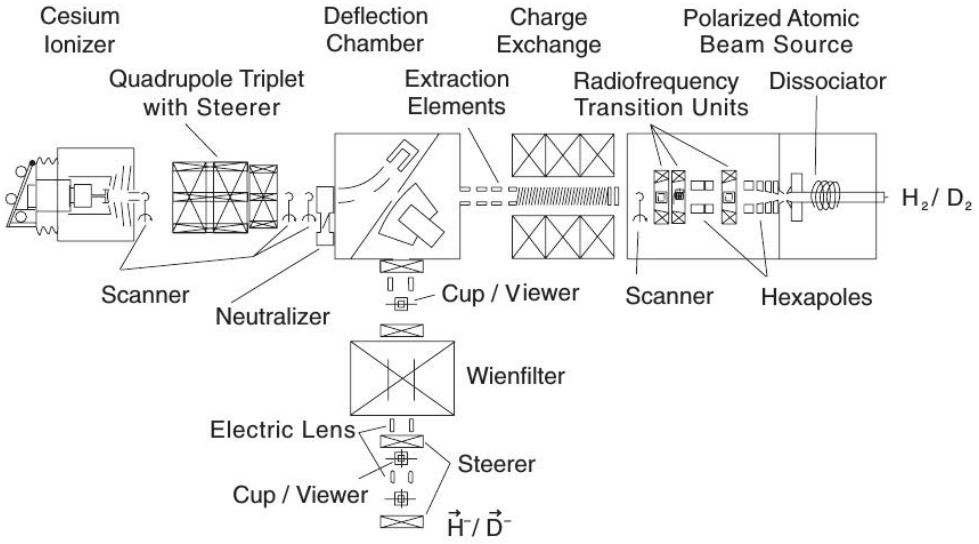

Figure 2.3: The left branch of the T-shaped configuration produces the caesium beam, while the right branch produces a polarised beam of hydrogen or deuterium atoms. The collision's negative ions are collected through the branch at the bottom of the image.

F is no longer an appropriate quantum number in larger fields because J and I couple more strongly to the external field than to each other [39, 41]. The

critical field is defined as follows:

$$B_{crit} = \frac{\Delta W}{(g_I - g_J)\mu_B}, \tag{2.7}$$

where ΔW indicates the hyperfine splitting in the absence of a magnetic field, μ_B represents the Bohr magneton, and $g_I - g_J$ are the nuclear and electron g-factors. The numerical values for protons are $\Delta W = 5.8 \cdot 10^{-6}$ eV and $B_{crit} = 50.7$ mT, while deuterons have $\Delta W = 1.4 \cdot 10^{-4}$ eV and $B_{crit} = 11.7$ mT.

The quantum numbers of the hyperfine states of hydrogen and deuterium for weak and strong fields are shown in Tables 2.1a and 2.1b. The states are numbered from most energy to least energy.

	$B \ll B_{crit}$		$B \gg B_{crit}$	
State	F	m_F	m_J	m_I
1	1	1	½	½
2	1	0	½	-½
3	1	-1	-½	-½
4	0	0	-½	½

(a) Hydrogen

	B<<B_{crit}		B>>B_{crit}	
State	F	m_F	m_J	m_I
1	3/2	3/2	½	1
2	3/2	½	½	0
3	3/2	-½	½	-1
4	3/2	-3/2	-½	-1
5	½	-½	-½	0
6	½	½	-½	1

(b) Deuteron

Table 2.1: Hyperfine states [41]

As Hempelmann describes in [39] Fig. 2.4 and 2.5, the beam is unpolarised if all states are equally occupied. Changing the relative occupation yields polarised beams. The atoms enter a magnetic hexapole after passing through the nozzle. The strong magnetic fields in the hexapole act on the electron dipole moment J, producing a focussing force for states with positive m_J and a defocusing force for those with negative m_J. The resulting beam is polarised in the radial direction as the defocused components are removed. In large fields, however, the net nuclear polarisation of the remaining hyperfine states is zero, as seen in the diagrams.

The relative occupation of the hyperfine states is modified through three Radio Frequency Transfers (RFT) to generate a nuclear polarised beam. These are composed of a tunable magnetic field that splits the hyperfine energy

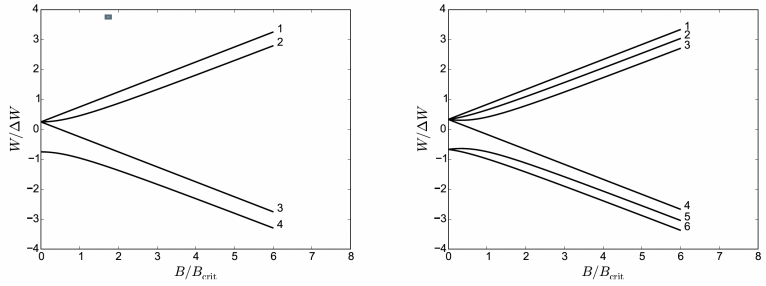

Figure 2.4: Hyperfine states as function of magnetic field, Hydrogen (left) and deuterium (right) [39].

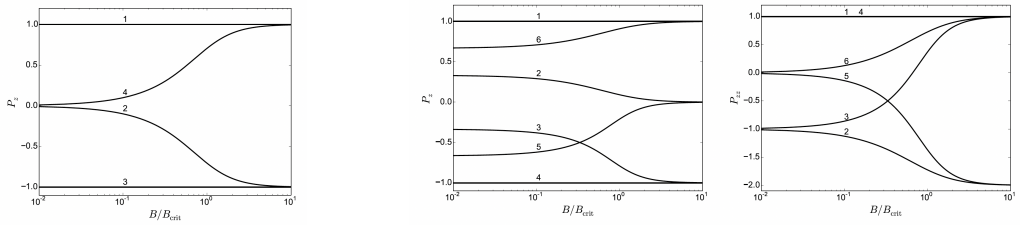

(a) Hydrogen (b) Deuterium, P_z (left), P_{zz} (right)

Figure 2.5: Polarisation of the hyperfine states as function of the magnetic field for H and d [39].

levels and a radio frequency electromagnetic pulse that induces transitions between them. Using different combinations of RFTs, different combinations of vector and tensor polarisation can be created, as shown in [42]. By transferring particles from state 1 to state 4, for example, a deuteron state with a vector polarisation of $-2/3$ and a tensor polarisation of zero is obtained. RFTs are imperfect in practice, resulting in lower polarisations. After each COSY cycle, the polarisation state is usually modified.

The caesium beam is the second component of the polarised source. To obtain an appropriate cross section for the charge exchange reaction, the caesium atoms are first ionized at the surface of a porous tungsten button and then electrostatically accelerated to roughly 45 keV. The ionized caesium beam is subsequently neutralized in a caesium vapour cell.

Any ions that remain in the beams are deflected to the side. In a central charge exchange area, the neutral caesium beam and the polarised atomic beam meet inside a solenoid that determines the spin quantization axis. The

magnetic field is strong relative to the critical fields of protons and deuterons, reaching up to 200 mT. Negatively charged ions can be obtained via the charge exchange process H + Ce $\longrightarrow$ H^- + Ce^+. Finally, the polarised beam goes through a Wien filter, which turns the spin to match the ring's magnetic field direction.

2.4 EDM search at COSY

Because COSY is a completely magnetic ring, there is no way to employ the *Frozen Spin* condition, and the particle's revolution frequency and the spin's precession frequency will differ. This will result in a small oscillation of the vertical polarisation rather than a polarisation buildup. A Radio Frequency (RF) Wien filter [43] can be used to observe polarisation accumulation. The RF Wien filter provides a perpendicular to the beam electric and magnetic field that oscillates at a predetermined frequency. The electric and magnetic fields are adjusted in such a way that the Lorentz force on the particles disappears and does not interfere with the particle's beam path or momentum. Rather, it will only have an impact on the particles' spin. It will give the particles' spins a slight kick, influencing the spin precession in the accelerator. The RF Wien filter's operating frequency must be a harmonic of the spin precession frequency and may be chosen using equation 2.8 :

$$f_{RF} = k \times f_{rev} + f_s = (k + \gamma \cdot G) f_{rev}. \tag{2.8}$$

Where f_{RF} stands for RF Wien filter frequency, f_{rev} for the COSY revolution frequency, k for the harmonic order (integer), γ for the Lorenz factor of the particles and G for the anomalous magnetic moment. RF Wien filter at COSY uses in most of the cases the set of harmonic $k = 1$ with a frequency of 871 kHz [44] for deuterons with a momentum of 0.97 GeVc^{-1}. When RF Wien filter operates at that values of harmonic, it affects the spin in a way that it will preferentially get a direction while precessing in the horizontal plane [45]. Due to the preferred spin direction, the Wien filter generates a gradual build-up of vertical polarisation, which is dependent on the EDM and so produces a detectable signal.

2.5 Spin coherence at COSY

Since COSY uses a fixed magnetic field for bending the particles, and the spins of the particles are lying on the ring plane, they undergo precession at a specific frequency of 120 kHz [46].

Given this fact, in order to measure additional polarisation effects the spins of the particles must remain coherent during the precession. This calls for the need to measure the so-called "Spin Coherence Time" (SCT), which is defined as the time taken for the resultant spin vector to reduce its magnitude by a factor $\frac{1}{e}$. To measure SCT using a polarimeter the measurements must be timed such that at every measurement the spins are expected to be aligned in the same direction. So the introduction of a "time stamp system" is needed to record the horizontal polarisation as a function of time.

In this setup a beam that stays coherent will have a clear pattern of asymmetry in the vertical direction, and decoherence effects will manifest as a gradual movement towards symmetry. On the other hand EDM effects will cause a build-up of a horizontal asymmetry, but only if the beam stays spin-coherent. Because in an incoherent beam the average value of the vertical polarisation build up will be zero, since the precession of many of the particle will be out of sync with the Wien filter frequency.

Chapter 3

JEDI POlarimeter - JEPO

The JEDI POlarimeter (JEPO) is a modular calorimeter made of a matrix of LYSO scintillating crystals coupled with SiPMs. To measure the polarimetry JEPO exploits elastic scattering of charged particles on a carbon target, measuring its asymmetry.

A schematic view of the detector is given in Fig.3.1.

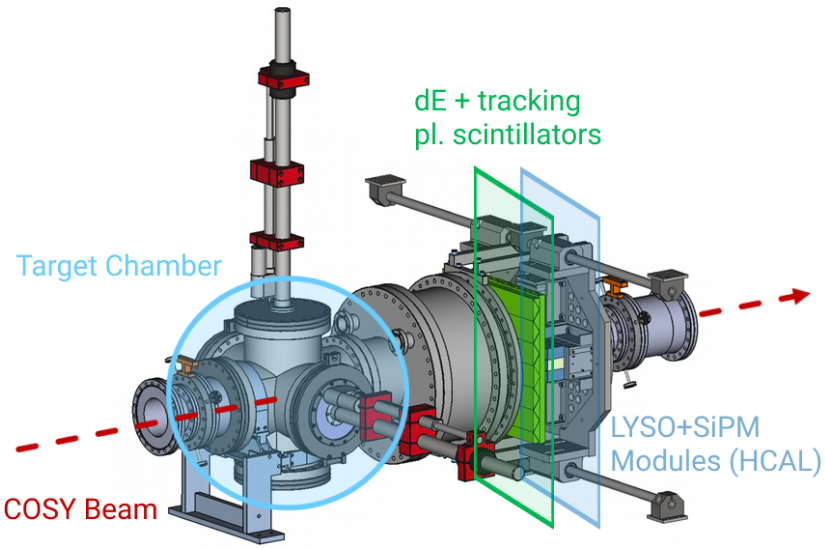

Figure 3.1: Schematic representation of JEPO. The beam, coming from the left, hits on the target chamber and is scattered, crossing first the tracker, then the LYSO calorimeter

The polarization cross section for a charged particle that scatters elastically on a carbon target can be written as :

$$\sigma_{pol}(\theta, \phi) = \sigma_{unpol}(\theta) \left[1 + p_y A_y(\theta) \cos \phi\right] \tag{3.1}$$

where p_y is the vertical polarisation. In case of spin-1 deuterons, an additional factor of 1.5 appears multiplying the pA term.

From the Eq. 3.1 an asymmetry arises, in case of an upwardly polarized projectile the gradient in scattering rate is in left-right direction (L/R), as can be seen in Fig. 2.3.If this pattern is rotated by 90°, measuring a sideways polarisation, it would bring about an up-down (U/D) asymmetry.

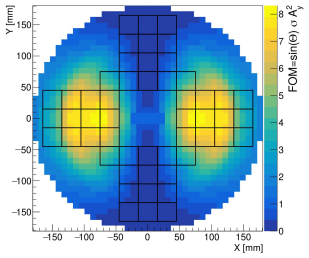

Figure 3.2: Polarimeter figure of merit from d+C elastic scattering [47].The 52 LYSO crystals employed in the current design of the EDM polarimeter are indicated by the black lines.

This chapter describes the concepts that lead the development and the design of the **JE**DI **PO**larimeter. Its main components, the LYSO crystals and the SiPMs, are presented in detail.

The end of this chapter treats the LYSO modules that make up the detector. These modules have been tested and simulated to understand their behaviour and performances in Bragg peak estimation and energy resolution, thus leading to particle identification and spin measurement.

3.1 Detector scheme

The JEPO detector is based on 52 LYSO crystals modules coupled with SiPMs that covers the most useful region in terms of polarimeter statistics (an array of 3x4 modules each side plus one in the corner as shown in Fig. 3.2) . The crystals are 3×3×8 cm^3 mounted with their long axis parallel to the beam. The modules development was guided by the following factors:

- **Module simplicity**
  The lesser components utilized to construct the modules, the less liable

they are to error. Within the same reasoning, a single detector layer design was chosen to simplify the data analysis.

- **Interchangeability**
  If one of the modules fails, the others can be swapped out quickly. This also means that the final polarimeter assembly should only include one type of module.

- **High Resolution**
  Because the primary goal of a polarimeter is to identify and quantify elastically scattered particles, a high resolution aids in distinguishing the elastically scattered from other ones. For the same reason, an absorber in front of the module was rejected out, as it would allow a smaller scintillator to be used while lowering the resolution.

- **Long term stability**
  It is critical that the performance of this polarimeter does not vary over time because it will be used to measure polarisation in a high-precision long-running experiment. As a result, the scintillator LYSO was chosen. It has good radiation durability, and its temperature-dependent light yield loss of $0.28\%^{\circ}\mathrm{C}^{-1}$ in the region of 25 to 50 degrees Celsius is moderate [48].

- **Whole detector setup simplicity**
  To keep the overall detector assembly and data acquisition (DAQ) system to a minimum, no signal amplifiers were used between the photon detector and the analog-to-digital converters (ADC), as they could be a source of noise and non-linearity. Furthermore, SiPMs were chosen over PMTs because the latter required a separate high-voltage source for ea ch module.

3.1.1 LYSO Crystals

LYSO ($Lu_{1.8}Y_{0.2}SiO_5$:Ce) is a Cerium-doped Lutetium Yttrium Oxyorthosilicate inorganic scintillating crystal. This is a commercially available ([48–50] type of scintillator with ideal properties for an EDM calorimeter.The light output is higher than the most common inorganic scintillator (32 γ/KeV) and the time response is fast enough to be well read by SiPMs ($\sim$ 40 ns at

420 nm). In comparison to organic scintillators like plastic ones, inorganic scintillators are still slower. A common plastic scintillator, such as the NE 104, has a decay constant of 1.9 ns, whereas a NaI(Tl) crystal has a decay constant of 230 ns [51].

This type of scintillating material is built from a crystalline complex and forms a band-structure in the energy-momentum space. A ionizing particle passing trough the crystal may cause an excitation in the valence band electron that moves to the conduction band leaving a hole in the valence one. One electron-hole pair requires roughly three times the energy of the band gap [52]. In principle, electrons and holes can easily move inside their respective bands. A photon is released out from scintillator if recombination (i.e., the electron jumps back into the valence band) happens. Scintillation is the process that turns the deposited particle energy into light. Direct de-excitation from the conductive into the valence band releases photons that are typically in the ultraviolet range. An electron and a hole, on the other hand, may only recombine if their respective momentum vectors add up to zero (momentum conservation). This might cause a low recombination half-life in a pure crystal, leaving the scintillator ineffective at high rates. Impurities or dopants are introduced into the crystal to solve this problem. In the band gap between valence and conduction bands, they contribute intermediate energy levels. These trap states have the ability to pick up a hole from the valence band and hold it until an electron with a matching momentum vector can be trapped and form a neutral but excited state [52]. If the dopant material is selected appropriately, the de-excitation of this state will release photons that are in the visible spectrum and may be detected by a photon detector.

The most significant result of this effect is that the scintillator's absorption and emission spectra will not overlap, making it transparent to its own scintillation light. An electron can be excited into the so-called exciton band, where it forms a weakly bonded system with the hole, which is known as an exciton (a scheme of it is shown in Fig. 3.3). If an exciton is captured in an impurity trap, it can recombine instantly, lowering the inorganic crystal's overall decay constant even more.

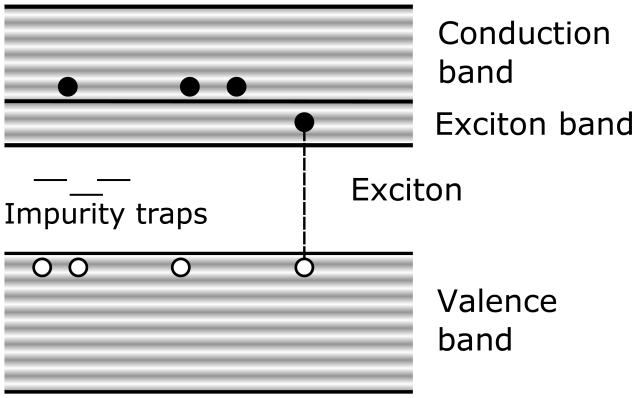

Figure 3.3: In the energy-momentum space, the band structure of an inorganic scintillator crystal. Ionizing particles create free electrons and free holes, which can recombine utilizing impurities in the crystal lattice's intermediate energy states in the band gap (traps). Excitons, which are slightly bonded electron-hole pairs, can also be generated. Recombination is accelerated since they travel in pairs.

The primary benefits of an inorganic scintillator over other kinds of scintillators, such as organic plastics or gaseous, liquids, or glasses, are the greater stopping power and the high light output of all scintillator types. Unfortunately, most classical inorganic scintillator crystals, such as NaI, CsF, LiI(Eu), and KI(Tl), are hygroscopic and must be tightly sealed to protect them from atmospheric moisture. Other (newer) crystals, such as BGO, BaF2, and LYSO, do not have this issue and may be handled more easily.

The stable isotope $^{175}_{71}$ Lu constitutes 97.41% of naturally occurring lutetium, whereas the isotope $^{176}_{71}$Lu makes up 2.59 percent [53]. The latter is a long-lived radioisotope that β^--decays into $^{176}_{72}$Hf with a half-life of $\approx 37.6 \times a\ 10^9$ years [54].
This decay is observable in the LYSO crystals' low energy spectra [55], but because the endpoint energy of the electron from the β^--decay is 1193 keV, it has little effect on measurements of deuterons in the hundreds of MeV range.

LYSO is a relatively recent (patented in 2003 [56]) non-hygroscopic, inorganic single crystal scintillator with remarkable qualities including a small decay

constant, high density, high light output, and a response spectrum that fits the sensitivity profile of PMTs employing bi-alkali photo-cathodes as well as SiPMs. It is also extremely radiation-resistant. Irradiation tests on LYSO samples utilizing gamma radiation doses up to 10 kGy revealed light output losses of only 12%, which is significantly less than previous high-energy physics crystal scintillators. Furthermore, it was demonstrated that annealing at 300°C restores the radiation-induced losses.

Even at room temperature, this recovery occurs, although at a somewhat slower rate [57]. Table 3.1 summarizes the characteristics of Saint-Gobain's LYSO crystals. All of these characteristics make the LYSO scintillator crystal an excellent candidate for constructing small detector modules employed in JEPO.

Density	7.1 g/cm
Wavelength of emission (max)	420 nm
Refractive index @ max emission	1.81
Decay time	36 ns
Light yield	33.2 Kphotons/MeV

Table 3.1: LYSO crystal properties from Saint-Gobain's data-sheet [48]

The current configuration consists of 52 such crystals, 48 of which are placed in 4×3 arrays along the four x and y axis spreading out from the center, as seen in figure 3.2. Scattering angles of 4 to 15 are covered along the axes. Figure 3.4 depicts a completed module sketch, as well as an open view of the readout end and pieces for a second full detector.

The module's length is 14 cm. A 1 mm thick optical silicon interface connects the crystal to the SiPM array [58], a 20 μm pixel SiPM readout array of the SensL J-series [59]. A custom-made passive summarizer PCB adds up the charge from all 64 separate SiPMs for the array's readout. The crystal is first wrapped in a 50-μm white Teflon reflecting sheet, then in 50 μm black Tedlar sheet for optical isolation [60]. Two strips of 25 m Kapton are wrapped around the end of the LYSO crystal and pulled along the side to hold the entire assembly together before being held in place and tensioned with a circular wave-spring at the end. References [47, 55, 61] provide more information.

Figure 3.4: A design and construction sketch and disassembly photos for a LYSO crystal detector, with colour to show the major components. The LYSO crystal's corners are chamfered to create a stable mount against the aluminium housing that holds the SiPM, as indicated by the red arrows. The labels stand for: (1) LYSO crystal; (2) SiPM array (88); (3) housing and mechanical system; (4) wrapping with three layers: Teflon as a reflector, Tedlar for light tightness, and Kapton [60] for mechanical stability.

3.1.2 Silicon Photon Multipliers (SiPMs)

The photo-diode is the basis of all silicon-based semiconductor photon detectors. A PIN-diode, is a semiconductor photo-diode that is doped positively over one side (p-layer) and negatively on the other (n-layer). The middle (intrinsic) layer is either not doped at all or is just minimally doped. The PIN-diode is reverse biased, and generates an electric field in the intrinsic layer, in contrast to the normal functioning principle of a diode. Electron-hole pairs are formed when a photon passes through the diode's thin top p-layer and deposits its energy in the intrinsic layer. These pairs proceed along the electric fields to the diode's opposite poles, providing a current proportional to the energy of the photon.

The ***A****valanche* ***P****hoto-****D****iode* (APD) is one particular advancement of a PIN-diode. A heavy doping is provided on both sides, a positive layer (p^+-layer) on the top side and a negative layer (n^+-layer) on the opposite side make up this sort of photo-diode. A less highly positive layer (p-layer) is set

just in front of the n^+-layer. Between the p^+-layer and the p-layer is the intrinsic layer. This configuration produces a minor electric field gradient in the intrinsic layer (drift area) and a significant field gradient between the p-layer and the n^+-layer (avalanche region) when reverse biased (See Figure 3.5).

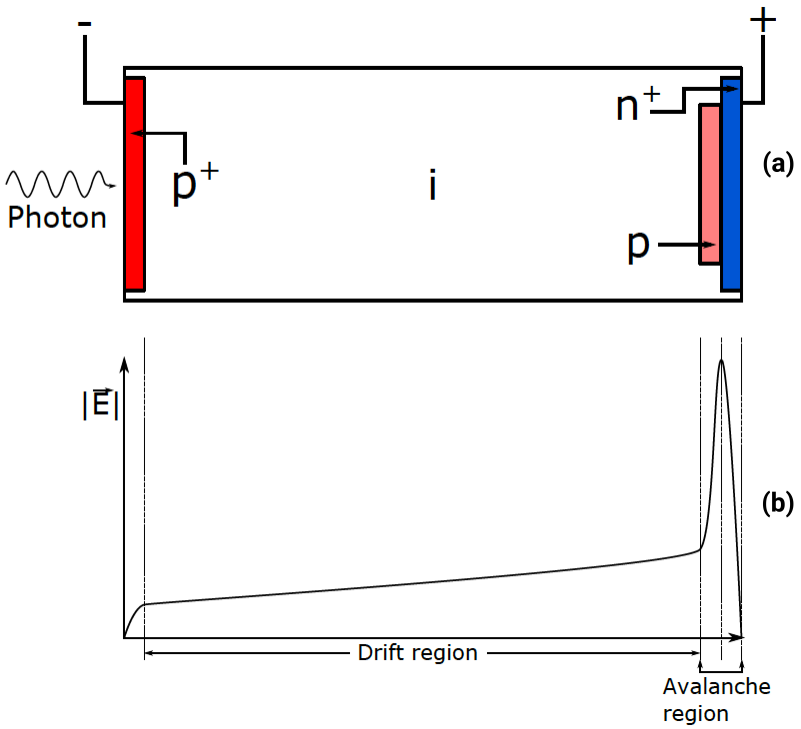

Figure 3.5: An APD is shown in a schematic diagram. (a) The cross section is shown to illustrate the APD's layers. The electric field within the diode can be seen in (b).

The penetrating photon forms electron-hole pairs in the drift zone, just as it does in the PIN diode. The electrons are drawn to the avalanche zone by the electric field gradient. The electrons in this region are pushed by the strong field gradients until they accumulate enough energy to form secondary electron-hole pairs, which are further accelerated and make even more electron-hole pairs. When compared to a simple PIN-diode, this results in an avalanche of charges and a significantly higher current. An APD's signal gain can be hundreds of times more than that of a PIN-diode [52].The gain is related to the amount of reverse voltage supplied to the APD. The gain is split

into two ranges in such a reference to gas detectors. The signal generated by the APD is proportional to the amount of photons in the proportional gain range, whereas in the Geiger-mode, each photon generates the maximum potential current through the diode regardless of its energy. Once activated by a photon, the current flow persists in this phase. As a result, a quenching resistor has to be connected in series with the APD. Thanks to its quantum efficiency (about 80% [52]) APD is an excellent photon detector.

SiPMs are composed of micro-cells, which are two-dimensional arrays of small APD cells (down to 15 μm edge length [62]). Individual APDs have their anodes and cathodes coupled in parallel, and each APD can have its own quenching resistor wired in series or the entire SiPM array can have a single quenching resistor. The APDs are set into Geiger Mode by supplying an appropriate reverse bias voltage to them. Each photon that hits a micro-cell in this configuration triggers it to go into full current breakdown. Because the signal from a SiPM is made up of the sum of signals from each micro-cell, it is proportional to the number of activated cells and, as a result, to the number of recorded photons. Since the number of photons produced in a LYSO crystal is proportional to the deposited energy, a LYSO scintillator optically connected to a SiPM provides a signal that is directly proportional to the amount of deposited energy within the crystal. A SiPM's signal is a current which can be converted to a voltage signal by connecting the quenching resistor in series with the SiPMs, as shown in Figure 3.6.

The SiPMs employed during the construction of LYSO modules for JEPO were SensL J-Series arrays [59]. The array of sensors J-300210*64P-PCB is based on a 3×3 mm^2 array of SiPM MicroFJ-30020-TSV series, each with 20 μm pixels [59]. The dead time for delivering charge to the summing circuit is roughly 50 ps. Each pixel can deliver charge many times during the 40 ns decay time of the LYSO crystal [63].

3.1.3 DAQ system

Fast, high-resolution sampling ADCs (Struck 250-MSPS, 14-bit ADCs [64]) were used in the data acquisition system to decrease the dead time. A synchronized clock is used to manage the sampling. The photon signal has a time stamp for each channel and is split into eight integrals using the digitized

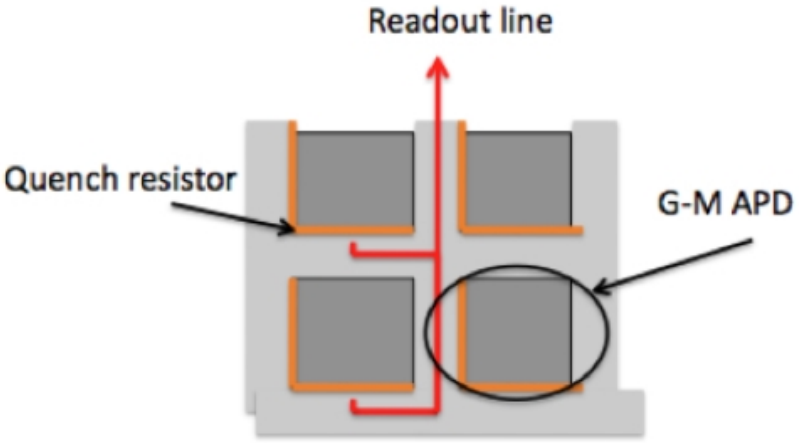

Figure 3.6: Scheme of a SiPM readout, the Geiger Mode APD is read out connecting it with a quenching resistor.

raw signal (see Fig. 3.7). The sampling ADC module contains an FPGA chip that can do this. Doing so it cuts down on the amount of data transfer required for each occurrence. Background level subtraction is possible with the two channels before the pulse, and their comparison acts here as pileup check. After background subtraction, the remaining six integrals are added together to provide the total charge recorded for an event.

A cut can be established in front of the LYSO module using a plastic ΔE scintillator, which emphasizes the appearance of the energy information associated with elastic scattering. The ΔE readout is comparable to the energy readout from the calorimeter module. The elastic peak may be chosen by setting a limited acceptance on the ΔE pulse height. In Fig. 3.8, the findings for three distinct deuteron beam intensities are combined. The characteristics of elastic scattering detection are shown in the panel of Fig. 3.8a, which include a narrow peak at the top deuteron energy and a tiny low-energy tail with no features. Because of their ΔE signal, deuterons reached the detector as elastically-scattered particles. Using a plastic ΔE scintillator, a slit may be created in front of the LYSO module, enhancing the appearance of the energy information associated with elastic scattering.

In the LYSO crystal, lower signal heights represent interactions with the crystal itself. The percentage resolution, which is on the order of 1%, is

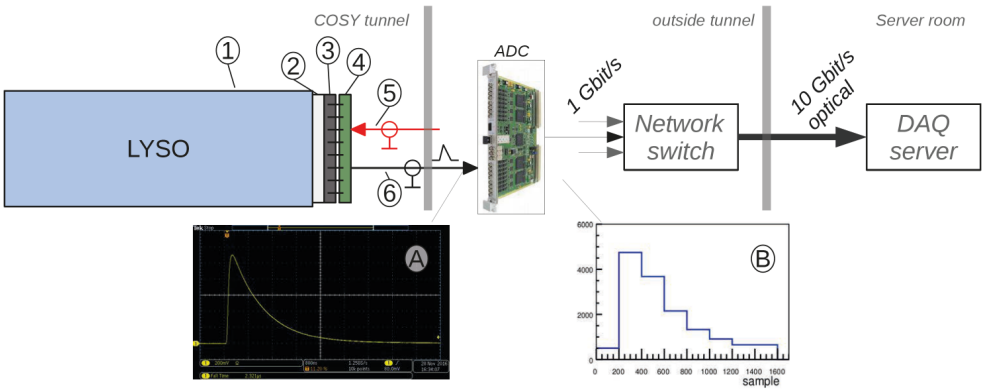

Figure 3.7: LYSO DAQ system scheme: ① LYSO scintillator crystal, ② optical coupling, ③ SiPM array, ④ PCB readout, ⑤ voltage supplied by coaxial cable and ⑥ analog readout by coaxial cable. The fast sampling ADC is coupled to the analog information stream. This digitized data is sent to the data acquisition server through a network switch. Panel Ⓐ displays the original analog signal, whereas panel Ⓑ depicts the eight integral outputs that resulted.

represented in the right panel (c). The relationship to increased particle energy is not linear, as shown in the central panel(b). This is a side effect of using SensL arrays. The SensL response is compared to that of Ketek [65] SiPMs with two different pixel sizes in Figure 3.9. The reaction of Ketek is linear. At the moment not all SiPM chips have been replaced because the polarimeter just requires that the elastic scattering events be identifiable.

3.2 Testing and simulations for LYSO modules

Since the beginning, efforts to do an EDM experiment with the COSY beam have focused on deuteron beams [66], due to the potential that any new EDM observation would happen at a higher sensitivity level for this particles [67]. This part of the study describes experiments conducted to better understand the detection efficiency, energy loss characteristics, and detailed crystal response of deuterons with energies less than 300 MeV.

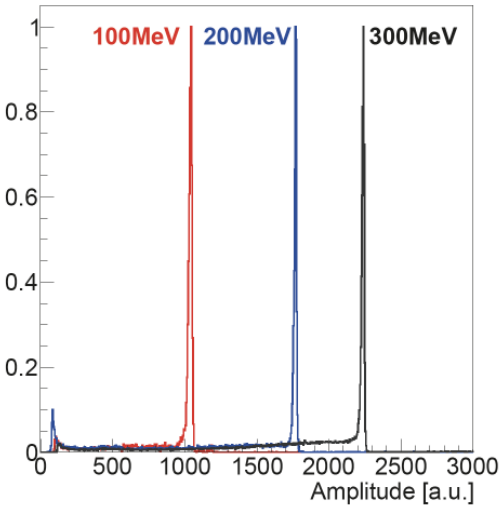

(a) LYSO module energy peaks at the tree different energies

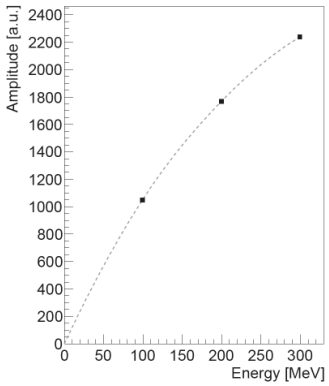

(b) Pulse height amplitude for the three different energies, with a line guide to follow the behaviour

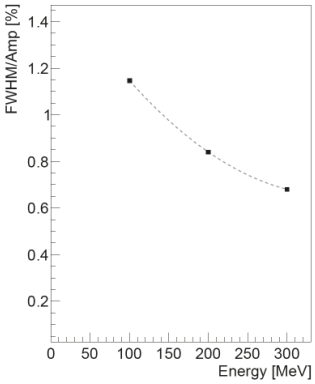

(c) Percentage resolution for the three energies, with line guide.

Figure 3.8: LYSO module response at 100, 200. 300 MeV deuteron beam gated by a window on the ΔE signal

3.2.1 Efficiency of deuteron reconstruction

The deuteron is a proton-neutron light-bonded system. It has a binding energy of 2.224 MeV, which is just ∼0.11% of its mass energy of m_d = 1875.612 MeV [55]. When a deuteron collides with another nucleus, it is quite likely to split apart into its constituent nuclei.

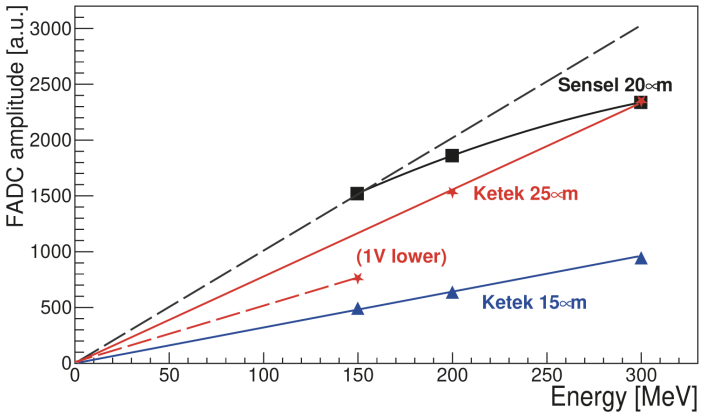

Figure 3.9: Linearity of several types of SiPM arrays in LYSO-based detector modules. The recorded signal's amplitude is displayed as a function of deuteron beam energy. In the case of Ketek-based modules, the relationship between amplitude and beam energy can be characterized by a linear function (solid line). It should be noted that the point at 150 MeV for the 25 m Ketek-based module was measured with a bias voltage that was one volt lower than the other point, and so cannot contribute to the linearity fit. With increasing beam intensity, the SensL-based modules depart from the linear behavior (dashed line). [55]

There are several areas where a break-up reaction may occur in a polarimeter that employs a carbon target for the polarimetry reaction and a heavy scintillator crystal. The target itself is the initial place where this interaction can occur. The deuteron beam will pass through the exit window of the beam pipe before hitting the target, depending on the setup, as it did in previous versions of the polarimeter development in the Big Karl region (another experiment at COSY). The target is within a vacuum chamber when the polarimeter is placed inside the COSY accelerator, and the scattering deuterons will pass through the exit window before hitting the LYSO-based detector modules. A break-up reaction might happen at any time, including at the exit window. Finally, the deuteron will pass into the scintillator crystal and will be able to break through the LYSO material.

The kinetic energy of a deuteron can be redistributed randomly between the proton and the neutron during a break-up process. The neutron is normally undetectable by polarimeter detector modules, while the proton, on the other hand, can be detected. Break-up-protons have an energy spec-

trum that spans the whole energy range up to the endpoint energy, which is equivalent to the kinetic energy of the projectile deuteron. However, it is extremely rare that the proton absorbs the whole kinetic energy of the initial deuteron, therefore the break-up proton peak does not overlap with the elastic deuteron peak, or just minimally overlaps with it. After a break-up reaction, the proton's angular distribution no longer reflects the original deuteron scattering angle. A proton produced by a deuteron's break-up process will no longer contain the asymmetry information from elastic deuteron carbon scattering and must be deleted from the study. The proton contribution to the elastic deuteron scattering energy spectrum can be removed using either a tight cut on the elastic deuteron peak or a cut in the ΔE vs. E plot where the deuterons and protons occupy distinct bands (see Sec. 3.2.5).

The scenario is different with deuterons within the LYSO crystal. They carry the asymmetry information from the polarimetry reaction and may also be exploited to measure the polarisation since they enter the detector module as a deuteron. The issue is determining what these occurrences are. They are positioned on a band that overlaps the proton band from the target's break-up protons in the ΔE vs. E plot and cannot be distinguished. The break-up protons from inside the scintillator are also eliminated by cutting the elastically dispersed deuteron.

The portion of deuterons that undergoes a break-up reaction within the LYSO scintillator in a configuration with nearly negligible contamination from other protons might be measured as a possible solution to this problem. To operate as a trigger, a very thin plastic scintillator with dimensions of 10mm x 10mm x 1mm is positioned in front of the detector module. Only deuterons that touched the LYSO scintillator in the very centre were picked, and events that would strike the modules at the periphery were deleted, ensuring that all deuterons were halted completely within the crystal. The energy spectrum obtained with this configuration was just of deuterons and protons that broke up inside the LYSO crystal during a break-up process. The break-up proton contribution of the exit window may be ignored since it is made of very thin (0:4mm) stainless steel. This spectrum for 250 MeV deuterons is shown in Figure 3.10. It's characterized by a big deuteron peak at the beam's energy, with the break-up protons in the background. The

spectra was separated into two ranges to determine the number of deuterons that underwent a break-up reaction. The deuteron peak was fitted using a Gaussian function, and the peak value was set to 100%. The *signal range* was defined as the range of the Gaussian between 90% and $+6\sigma$. This guaranteed that the whole peak was inside the acceptable signal range. The choice of 90% as the lower limit is arbitrary, but the results may be compared as long as this definition is applied to the spectra of all observed beam energies. The second range, the *full range*, was defined as the distance from the 0.5 percent mark to the end of the signal range, excluding any pedestal effects. The deuteron detection efficiency was calculated by dividing the number of occurrences in these two ranges and describes what proportion of the deuteron did not break up when halted by the LYSO crystal. After a cut on the elastically scattered deuterons was applied to retrieve the real number of deuterons that have struck the relevant detector module, the deuteron detection efficiency may be multiplied with the number of events, just like any other efficiency correction.

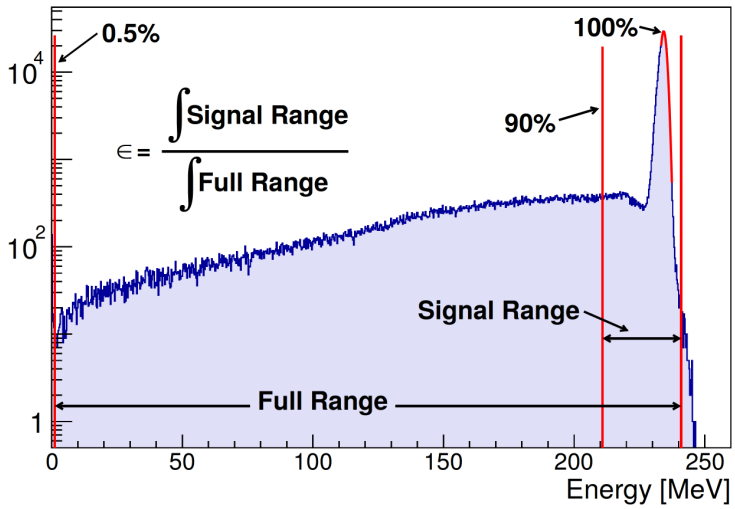

Figure 3.10: Reconstructed energy spectrum for a 250 MeV deuteron beam from light received by a SiPM at the crystal's back. The reconstruction efficiency is the likelihood that a deuteron will have a signal that contains more than 90% of its peak energy. The total number of occurrences recorded over a threshold of 0.5 percent is compared to this count rate. The LYSO detector was preceded by a 1 mm thick plastic event trigger detector.

Figure 3.11 depicts reconstruction efficiency for four different LYSO calorime-

ter modules. Each of these four sets of data is fitted with a colored line using an exponential curve. As the bombarding energy grows, all of the sets show the same diminishing pattern with rising energy, which is to be expected given the greater possibility of a breakdown encounter. The Geant4 simulated points and fit fall inside the four test measures' defined region. The Geant4 reconstruction efficiency simulation rolls over at energies below 100 MeV and gradually approaches one for very tiny kinetic energies. An exponential model would not follow this pattern below the range of Fig. 3.11. Up to a third of the events in the energy range where an EDM polarimeter would be utilized might fall beyond the 90 percent threshold used to identify elastic scattering. polarimeter target cannot clearly discriminate these occurrences. In a realistic deuteron EDM experiment, extreme caution would be required to guarantee that changes in the mix of event types would not alter the analyzing power associated with the tail below the elastic peak. In order to obtain additional information on the beam polarisation, their energy range could be included in the acceptance.

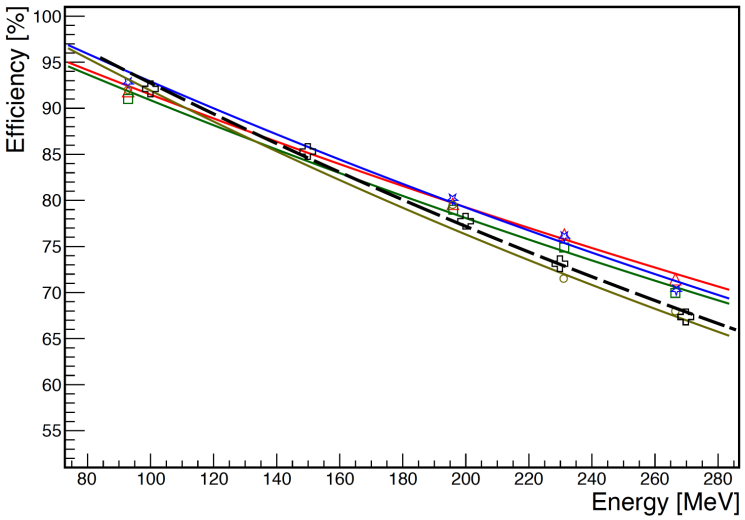

Figure 3.11: The multicolored points at 100, 200, 230, and 270 MeV represent the reconstruction efficiency of four distinct LYSO modules. The coloured lines are exponential fits to the matching set of points. The efficiency anticipated by a Geant4 simulation that incorporates deuteron breakdown is shown by plus signs, which are fitted by the dashed exponential decay curve.

3.2.2 Bragg peak estimation

Different mechanisms cause a particle's energy to be lost as it passes through matter. These processes are influenced by the particle type as well as the absorber material. The analysis of particle energy loss in this section will be confined to charged particles heavier than electrons in an absorber material with an average nucleus mass greater than the particle's. *E.g.* a deuteron passing through the LYSO scintillator crystal.

Inelastic collisions with the electrons of the target material atoms, elastic scattering of the material nuclei, emission of Cherenkov radiation, nuclear reaction, and bremsstrahlung are all mechanisms that cause a heavy particle to lose kinetic energy as it passes through matter. The first of these processes contributes by far the most to the particle's energy loss and was employed by Niels Bohr to develop a classical formula for a material's *stopping power*. When a particle with a particular kinetic energy travels a certain distance through a material, its stopping power determines how much energy is lost during the travel. It's frequently abbreviated as dE/dx , with dx denoting a unit of distance. Hans Bethe, Felix Bloch, and others adjusted Bohr's calculation to include relativistic and quantum mechanical effects, resulting in the famous Bethe-Bloch formula [51]:

$$-\frac{dE}{dx} = 2\pi N_a r_e^2 m_e c^2 \rho \frac{Z}{A} \cdot \frac{z^2}{\beta^2} \left[ln\left(\frac{2m_e\gamma^2\beta^2 W_{max}}{I^2} \right) - 2\beta^2 - \delta - 2\frac{C}{Z} \right], \quad (3.2)$$

where r_e is the classical electron radius, m_e its mass, N_a the Avogadro's number, ρ defines the density of the absorbing material, Z and A its atomic number and atomic weight. Then, z identifies the charge number of the impinging particle, I the mean excitation potential and W_{max} the maximum energy transfer that can occur in a single collision, $\beta = \frac{v}{c}$ and $\gamma = (1-\beta^2)^{-\frac{1}{2}}$. At the end, the density correction δ and the shell correction C are applied. The correction factor are important only for incident particles at very high or very low kinetic energies. Dr Leo describes it in detail in its book [51].

In the energy range of the deuterons of COSY the equation 3.2 can be simplified to:

$$-\frac{dE}{dx} = \pi N_a r_e^2 m_e c^2 \rho \frac{Z}{A} \cdot \frac{z^2}{\beta^2} \left[ln\left(\frac{2m_e\gamma^2\beta^2}{I} \right) - \beta^2 \right], \quad (3.3)$$

since $m_d \gg m_e$ and therefore $W_{max} \approx 2m_e\gamma^2\beta^2$. The following scaling rule (Bragg's Rule) may be used to estimate the stopping power of a mixed material (with a density ρ) such as LYSO:

$$\frac{1}{\rho}\frac{dE}{dx} = \frac{\omega_1}{\rho_1}\left(\frac{dE}{dx}\right)_1 + \frac{\omega_2}{\rho_2}\left(\frac{dE}{dx}\right)_2 + ...\frac{\omega_n}{\rho_n}\left(\frac{dE}{dx}\right)_n. \tag{3.4}$$

ω_n denotes the weight fraction of the various components, whereas ρ_n denotes the individual densities. The following formula may be used to compute the weight fractions:

$$\omega_n = \frac{a_n A_n}{A_{tot}} \quad \text{with} \quad A_{tot} = \sum a_n A_n. \tag{3.5}$$

a_n describes the number of atoms that have an atomic weight of A_n in one molecule of the absorber material. For LYSO, the number of atoms of its constituents is described in Section 3.1.1.

It was critical early on in the investigation of the LYSO modules to ensure that the energy loss estimates in Geant4 were adequate for LYSO. This was accomplished by measuring the energy loss curve using a pair of 15x30x80 mm^3 crystals. Each crystal was individually wrapped to keep it light-tight. They were arranged such that they replicated the size of a normal 10 centimeter crystal. A dual channel PMT [68] was used to read them out. The crystals were installed on a moving platform so that the external beam could pass through them both. The energy of the beam was 270 MeV. The energy sharing between the two LYSO crystals may be adjusted continually by changing the angle. Figure 3.12 illustrates the crystals' arrangement. To obtain comparative measurements, a second module with dimensions of 30x30x80 mm^3 (the standard shape) was attached.

Pulse heights were measured as a function of rotation angle in the crystal pair. A stopping power (dE/dx) curve may be drawn against the deuterons' penetration depth by determining the difference in deposited energy from adjacent pairs of observations. The effective path length as function of the angle of rotation α can be written as:

$$x_{15mm} = \frac{15\text{mm}}{\sin(\alpha)} \quad \text{for the first crystal,}$$
$$x_{30mm} = \frac{30\text{mm}}{\sin(\alpha)} \quad \text{for both crystals.}$$

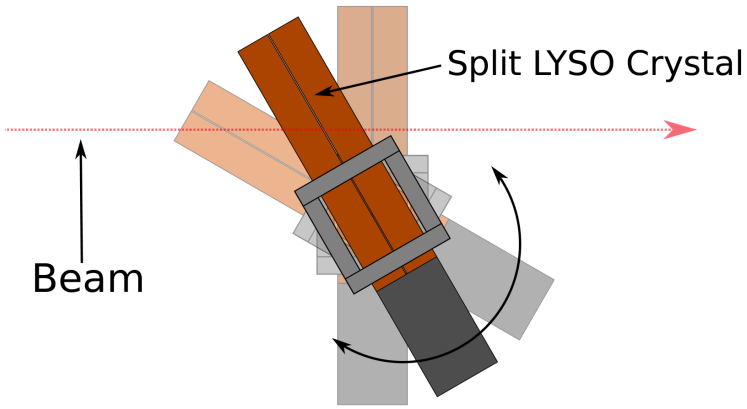

Figure 3.12: The energy loss measurements are set up as shown in the diagram. The beam's particles travel through both crystals. The path length in each module is continually altered by adjusting the angle. Each of the crystals has a deuteron path of $15/\cos(\alpha)$ cm, where α is the rotation angle.

The range of 20° to 90° can be covered by 11 different angle measurement with the setup in Fig. 3.12. Covering a penetration depth from 15 mm to 87.7 mm. In each measurement i, a couple of deposited energy and effective path length ($[x_{15mm}, E_{15mm}]_i$ and $[x_{30mm}, E_{30mm}]_i$) were obtained. Then the stopping power could be calculated by the difference between the energy deposit i and $i-1$:

$$\left(\frac{\Delta E}{\Delta x}\right)_i = \frac{E_{i-1} - E_i}{x_i - x_{i-1}} \quad \text{for} i \in [1, 11]. \tag{3.6}$$

Additionally, the first point: point *zero* $[x = 0$ mm, $E = 270\text{MeV}]_0$ had to be included to this set. Figure 3.13, where it illustrates observations of first crystal only (blue marker) as well as both crystals together (red markers) superimposed on a Geant4-calculated energy loss curve with its Bragg peak.The Monte-Carlo simulation was provided by Paul Maanen. The energy difference measurements obtained by comparing different angles correspond well with the estimated energy loss curve. This validates the use of Geant4 to investigate LYSO module performance in a polarimeter context.

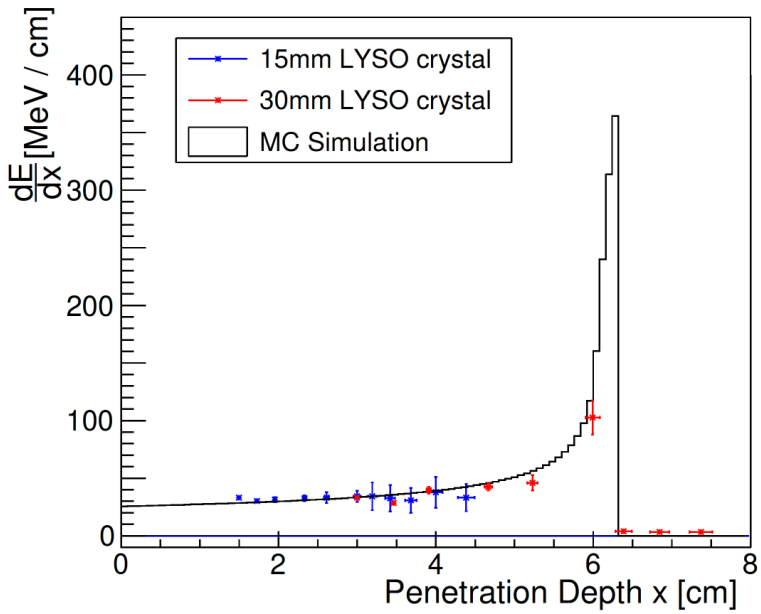

Figure 3.13: A graph showing the energy loss curve for 270 MeV deuterons in a LYSO crystal. The energy difference is represented as a function of the lower of the beam's initial and finishing penetration depths. The red points were taken using two LYSO crystals that were 30 mm in total thickness, while the blue points were taken with a LYSO crystal that was 15 mm thick.

3.2.3 Energy resolution

Energy resolution is one of the most important characteristics of any detector module. It determines how effectively one can discriminate between various processes such as elastic and inelastic scattering, as well as identify distinct particle species that hit the detector. The core purpose of a polarimeter is to identify the type of particle, as in the elastic scattering process, the particle recorded by the detector should be of the same type as the beam particle or the target in the case of inverse kinematics. Because the kinetic energy of an elastically scattered particle off a given target is only determined by the scattering angle, it is possible to predict how much energy will be deposited in a module at a particular angle to the target and the beam axis. Since the LYSO-based detector modules were intended to entirely absorb scattered particles, as said in the previous section (3.2.2), the energy deposited in the scintillator crystal equals the particle's whole kinetic energy at the time of entry into the detection module.

Each detector module's resolution was tested by placing it directly in the deuteron beam. The module was placed as near to the beam pipe's exit window as the setup permitted. The start counter and the target were taken out of the beam path. This operation was carried out for each installed module at each available beam energy in the associated beam time. The resultant energy spectra should only have one peak, which corresponds to the beam particles' deposited kinetic energy. In the case of a deuteron beam, there is a background that extends throughout the whole spectrum and is caused by deuteron break up processes inside the LYSO crystal [55]. The energy resolution describes how finely one particle's energy can be detected, or more precisely, what is the smallest energy difference between two particles that the detector can differentiate. So the resolution is proportional to the width of the peak and the position in the spectrum of this one. In the case of detector based on LYSO modules resolution R can be defined as follows:

$$R = \frac{\text{FWHM}}{E_{peak}} \sim \frac{\Delta E}{E}. \tag{3.7}$$

FWHM stands for *Full Width at Half Maximum* and E_{peak} is the position of the calibration peak in the energy spectrum. In the case of a Gaussian-shaped peak, the relation between the FWHM and the standar deviation σ is :

$$\text{FWHM} = 2\sqrt{2ln(2)} \cdot \sigma \approx 2.355\sigma. \tag{3.8}$$

If the calibration peak is perfectly Gaussian-shaped the resolution can be obtained by simply fitting it with a Gaussian and calculate the resolution from the fit. This approach, unfortunately, is impossible for the LYSO based detector, since it appears a double peak, well described in Müller's thesis [55]. As a result, a different strategy was chosen: all of the events collected for a certain calibration were filled into a histogram. The centre of the largest bin in the spectrum was used to determine the location of the calibration peak. Starting from this point, the bins to the left and right of maximum were found, when the peak first dropped below half of the maximum value. The FWHM for this peak was determined by the distance between these two bins. This strategy works for both clean and broadening or double-peak peaks. Figure 3.14 shows instances of two calibration peaks in two distinct modules with a 150 MeV deuteron beam. Figure 3.14a illustrates a module

with a very clean peak from which 3.14b shows a module with an obvious double-peak from which even a double-Gaussian fit fails to capture properly the form.The FWHM range is indicated by the black lines. This technique of estimating the resolution results in an underestimation of the real resolution of the module for modules that present a double-peak. Another option would have been to extract the resolution from only one of the two peaks, but it was agreed that the resolution extraction should reflect the real situation when the modules are utilized in the final polarimeter, therefore it is best to represent the worst-case scenario in this circumstance.

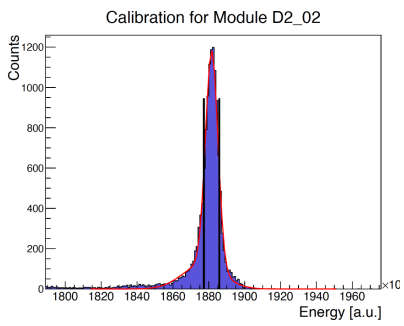

(a) Clean single peak example of a module signal.

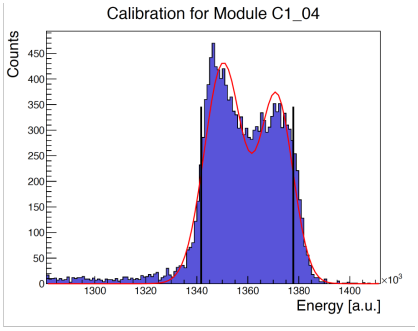

(b) Double-peak example of a module signal.

Figure 3.14: Energy spectra of two LYSO-based detector modules with a 150 MeV deuteron beam zoomed-in for calibration peaks. The black lines represent the FWHM area. The results of a single and double Gaussian fit to the peaks are depicted by the red lines.

For all LYSO-based detector modules, the resolution was computed using all accessible beam energies. The average of the energy-dependent resolution for both variants of the LYSO-based detector modules is shown in Figure 3.15. The dispersion in the resolution of the modules at the same energy can be fairly significant due to the variation in peak shape noted earlier, which is reflected in the broad error bars. The SiPM-based detector modules have a better resolution than the PMT-based counterpart. The value of the resolution reduces as the beam energy increases, i.e., the higher the energy, the better the resolution. The energy dependent-resolution was calculated using the following formula for both versions of detector modules [55]:

$$R(E) = \frac{A}{\sqrt{E}} \oplus \frac{B}{E} \oplus C. \tag{3.9}$$

This equation is commonly used to define the resolution of a calorimeter and thus may be used for LYSO-based detector modules, as they can be classified as calorimeter modules because they absorb all of the observed particle's energy. The quadratic sum is abbreviated by the $\oplus$ operator. Different qualities of a calorimeter may be described using the parameters A, B and C:

- A addresses the *Stochastic term* that includes the detector module's statistical fluctuations and electronic noise in the readout chain.
- B represents the *photon statistics fluctuations* that is due to inhomogeneity inside the crystal.
- C is the *energy-independent background noise* that can be related to a radiation damage component.

Analysing each item properly would be beyond the scope of this work. The fits, on the other hand, may be used to interpolate beam energy resolution between measured places.

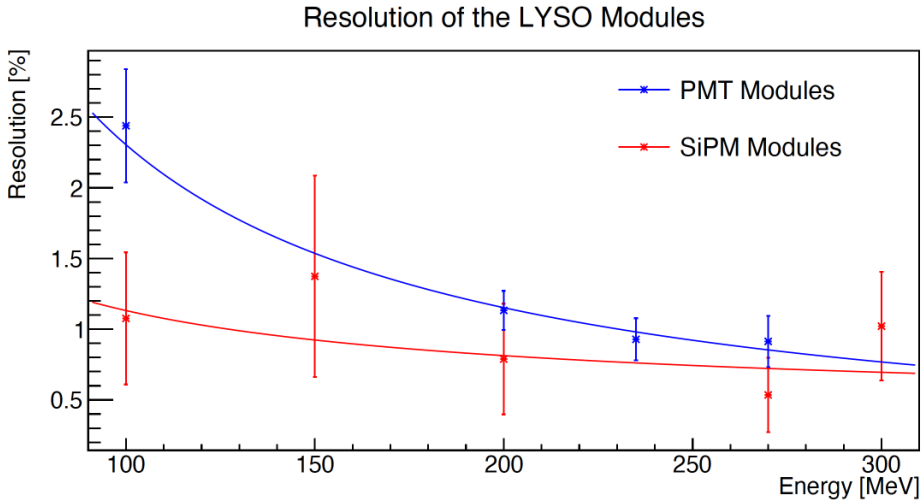

Figure 3.15: The mean of the energy resolution of both types of the LYSO-based detector units as a function of deuteron beam energy, using the Equation 3.9 to fit the points into the solid lines. The width of the resolution distribution is indicated by the error bars.

The observation, that the SiPM version of the LYSO-based detector modules has a very high resolution of less than 1% across the whole measured

energy range, is the most relevant outcome of the resolution measurement. The major purpose of the modules, which is the detection and counting of elastically dispersed particles, may be accomplished without difficulty at this resolution. Even when the modules exhibit double-peak behaviour, particle identification is still achievable without difficulty. It may be claimed that the great resolution of the modules was the main reason the double-peak problem was found. The calibration peaks from Figure 3.14 are shown in Figure 3.16, but this time they are not zoomed-in. The extremely small peaks show how good the modules' resolution is.

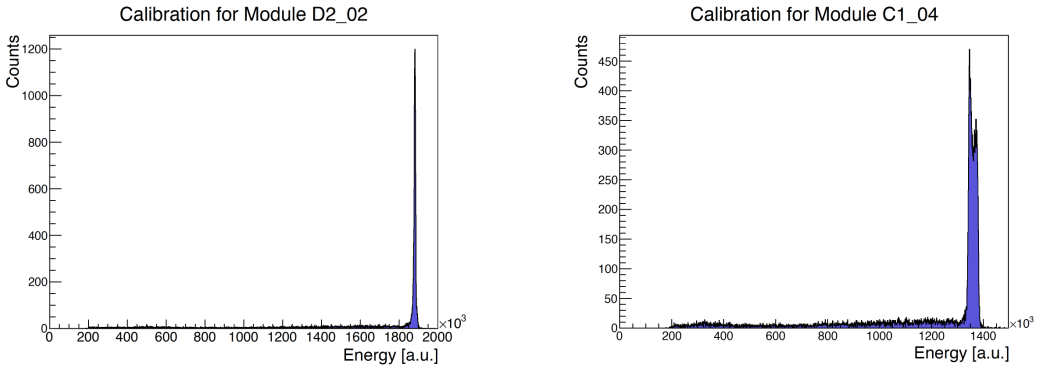

(a) Single peak example. (b) Double-peak example.

Figure 3.16: Calibration peaks of two LYSO-based detector modules with a 150 MeV deuteron beam. Full energy spectra are shown.

All LYSO-based detector modules were evaluated in the laboratory for light tightness and overall performance before being employed in the experimental setting. A test configuration based on a *Red Pitaya* [69] data collecting board was designed by David Mchedlishvili [70] . Each module was attached to this test setup once it was constructed, and a low-energy spectrum was measured. The radioactive lutetium ^{176}Lu isotope in a LYSO crystal decays via β-decay into the hafnium ^{176}Hf isotope. If the module is light sealed and the scintillator crystal is properly joined to the SiPM array, the emitted electron as well as the γ-lines from the de-excitation of the 176Hf isotope are observable in the low energy spectrum. A ^{22}Na and a ^{60}Co source were also employed to examine the modules. A spectrum like the one shown in Figure 3.17 is an example of this. This measurement can reveal if the module is not well packed or if the interface between the LYSO crystal is not ideal, requiring the module to be disassembled and rebuilt. The patterns in the

low energy spectrum that result from lutetium decay are identical to those described in the LYSO crystal data-sheet [48]. Performing this laboratory test ensured that the LYSO-based detector modules operate well in actual tests utilising the deuteron beam, and that no modules showed any signs of light leakage in any of the three rounds of the polarimeter development. An examination of the LYSO-based detector module's low energy resolution using the 511 keV peak yields a value of $\sim 15.3\%$. This helps to explain why there are no double-peaks formations in the low-energy spectra.

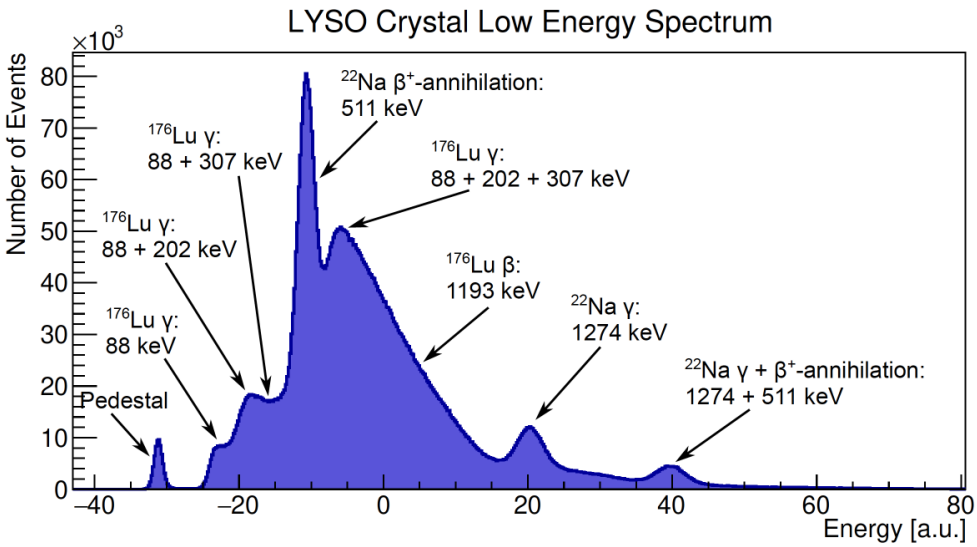

Figure 3.17: Low energy spectrum of a LYSO based detector module recorded in the laboratory. The continuous beta tail and three γ-peaks from the ^{176}Hf de-excitation are evident. Lund/LBNL nuclear data was employed to calculate the energy values [71]. A 22Na source was added to the module in addition to the internal radiation. ^{22}Na is a β^+ emitter, and the most prominent peak in the spectrum, which is situated at 511 keV, arises from one of the photons generated in the $\beta^+ + \beta^-$ annihilation. One γ-line is created by the ^{22}Na decay at 1274 keV [72], which is also easily recognizable. Since the LYSO crystal has such a huge volume, the chances of collecting several photons in a single event are rather high, resulting in peaks that reflect the sum of that multiple photons energies.

3.2.4 Front and side scans of the LYSO crystal

In order to better understand the double peak influence on the detector resolution another scan was performed on the modules and relative to the SiPM. Finally, all 52 modules were tested at 150, 200, and 300 MeV, resulting in varying depths of the Bragg peak. Figure 3.18 depicts sample data for one module. Figure 3.19 shows a scan from the side for a different module.

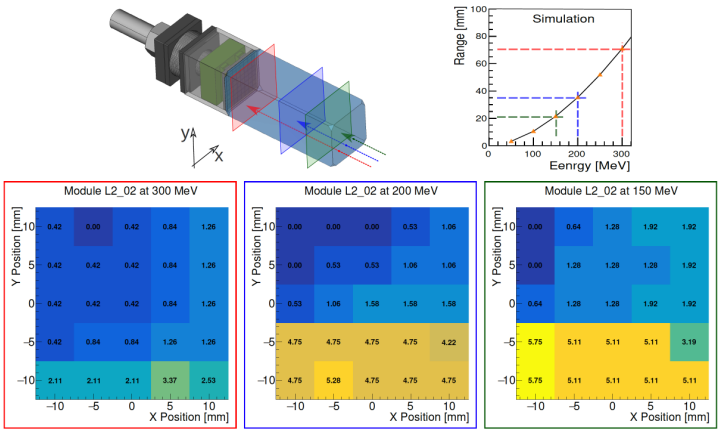

Figure 3.18: Relative energies measured in a grid of module $L2\_02$ at three different beam intensities. The percentage divergence of the observed pulse height from the data set's lowest value is shown by the numbers for each grid spot. The cells that have no variation are coloured in the deepest blue. The shades move from green to yellow as the variances increase. The most significant differences are around 6% (yellow). The depth of the Bragg peak is shown in a schematic of the module, which is also shown in a graph of range above.

These analyses indicated that the light emitted by the LYSO crystals is dependent on where the particle energy is deposited inside the crystal. Saint-Gobain [48] is the manufacturer of these crystals. Similar inhomogeneities were found for Epic-Crystals [49] and Tianle Photonics [50] crystals. When planning for crystal use and setting up acceptable thresholds on the elastic peak to employ during tests, this amount of variance must be taken into account.

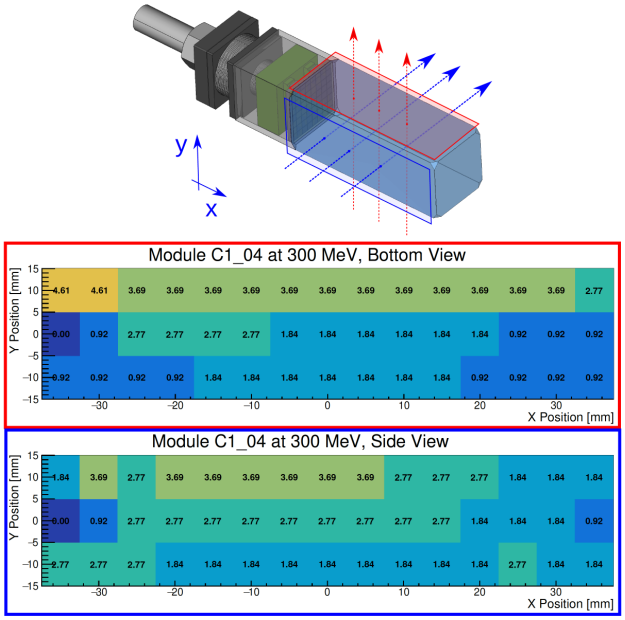

Figure 3.19: Results of scans made along the sides of module $C1\_04$ using 300 MeV deuterons. The energy peak indicates simply the energy lost in the crystal when these deuterons travel completely through it. As in Fig. 3.18, the data are expressed as a percentage shift from the lowest peak value (dark blue) to approximately 5% (yellow). For both sets of scan values, the graphic illustrates the direction of the beam flowing through the crystal.

3.2.5 Particle identification

An important information can be given by the ΔE vs. E spectra, produced by mounting an extra layer of plastic scintillator in front of the LYSO base detector modules. The type of particle may be determined using these spectra, and it is therefore an important tool for selecting the elastically dispersed deuteron required to calculate the beam's polarisation.

In order to improve the particle identification triangular ΔE detectors can be installed, which not only offer information for particle identification but can also be utilised to reconstruct the location of the tracks for individual events, by enabling the measurement of energy ratios over a continuous range (more about the reconstruction algorithm is described in 4.2). Before reaching the LYSO crystal, a particle passes through this scintillator and loses some of its kinetic energy. The initial results of a test employing this new detector is given in Chap. 4.

In a two-dimensional histogram, the energy loss in the plastic scintillator can be plotted against the total kinetic energy deposited in the LYSO crystal for each event recorded by the detector. The Bethe-Bloch formula, which is presented in Eq. 3.2, describes how much energy is deposited in the plastic scintillator based on the kind of particle and its kinetic energy. Figure 3.20 depicts a ΔE vs. E spectrum obtained in the second iteration of JEPO development [55] with a 2cm thick plastic scintillator positioned in front of a LYSO-based detector module at a polar angle Θ of 10° relative to the beam axis. The deuteron beam's energy was 300 MeV, and a 10mm carbon target was placed into the beam path. A particle's location on the ΔE vs. E spectrum is limited to a particle-specific band, regardless of its kinetic energy. These bands mimic the form of a banana in the case of protons and deuterons, hence they're frequently called the *proton-banana* and *deuteron-banana*, respectively. As can be observed in Figure 3.20, the deuteron band is placed above the proton band, and the heavier the particle, the more its corresponding band is pushed upright in the ΔE vs. E spectrum. The most energetic particles will be at the right end of their respective band, hence elastically scattered deuterons off the carbon target will be at the right end of each band. Every one of the events in this band are deuterons as well, but they also have lost their kinetic energy someplace else before hitting the detector rather than elastically dispersing off the object.The proton band hosts several events. Combining a thick target, high energy, and a large polar angle of the detector it resulted in a huge number of protons (coming from deuteron break-up in the target) being recorded. The protons from a break-up process can take any portion of the deuteron's initial kinetic energy, as mentioned in Section 3.2.1, and are therefore dispersed throughout the whole proton band. This spectrum also shows the deuterons that experience a break-up process within the crystal. In LYSO, the neutron event can only be found in the lower left corner of the ΔE vs. E spectrum.

An extra layer of plastic scintillator in front of the LYSO-based detector module can be extremely beneficial for selecting elastically dispersed deuterons for the estimation of polarisation. Only the elastically scattered deuterons from the LYSO energy spectrum may be selected by cutting around the elastic peak. The tail of the proton band, however, goes up to the elastic peak, as seen in Figure 3.20, if only the abscissa projection of this spectrum is

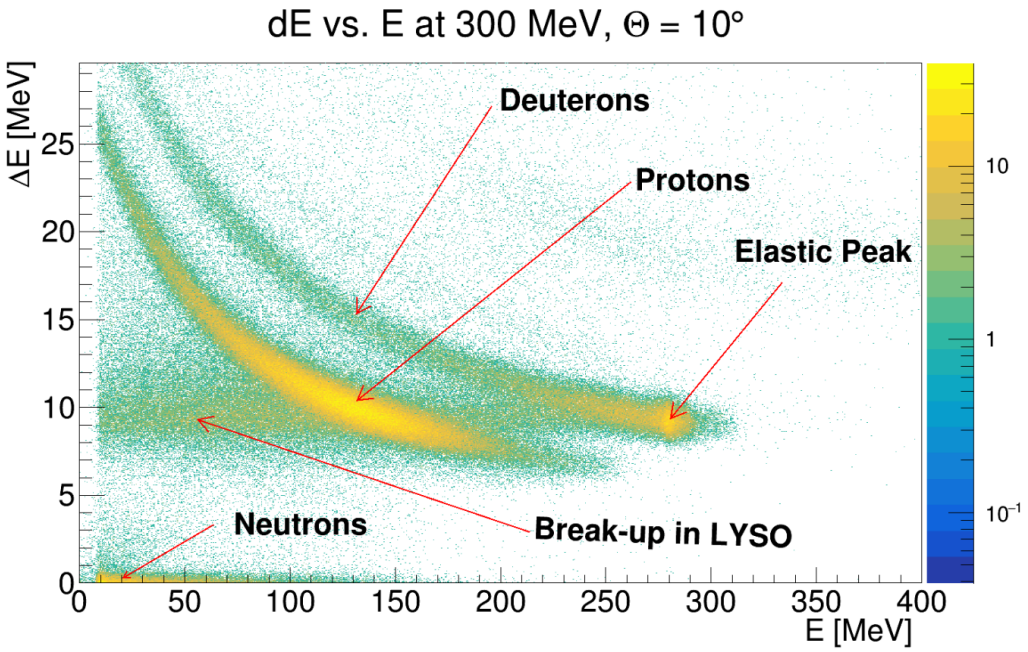

Figure 3.20: ΔE vs. E spectrum plot for a deuteron beam of 300 MeV scattering on a 10 mm carbon target [55].

provided. If no ΔE detector is placed, this is the situation. It is difficult to determine the lowest point of the cut if no elastic deuteron events need to be deleted while also excluding all protons. If a ΔEvs.E spectrum is available, a simple box cut around the elastic peak increases the amount of elastically scattered deuterons entering the analysis while reducing proton contamination. In addition, a second zone to the left of the proton band, surrounding the internal deuteron break-up band, can be defined to raise the number of acceptable events even further. As a result of these reasoning, it is clear that a ΔE detector must be included in the final polarimeter arrangement (see Chap.4).

Chapter 4

The SiPM Tracking Hodoscope - SiTH

As stated in the previous chapters, in order to improve the particle identification, layers of triangular ΔE scintillators (the **Si**PM **T**racking **H**odoscope - **SiTH**) can be installed. This detector will not only offer information for particle identification but can also be utilised to reconstruct the trajectories for individual events. In this chapter the design of this detector, as well as the guiding principle of the reconstruction of the events will be described.

In 2018 a Test Beam was performed on a prototype of this detector. A Geant4 simulation was planned to evaluate the performance of the whole SiTH. Firstly the simulation aimed to match the 2018 Test Beam configuration to get the same result, then subsequently exploit those parameters in the simulation of the whole detector. The results of Test Beam and simulations are shown in this chapter.

4.1 SiTH design

The angular coverage of each of the LYSO-based detector modules is quite large ($7.5 - 25°$). Since the unpolarized angular cross section is assumed to be constant over the polar angle Θ range of one module [55], a smaller angular binning for the computation of the polarisation would be preferable. As a result, an additional tracking detector in front of the LYSO-based detector modules to get the angle information of each event would be beneficial.

Reducing the angular binning of the existing polarimeter would be not compatible with the design requirement of it (see 3.1). However, as mentioned in the preceding sections, a ΔE detector is required in the final version of the polarimeter, hence the concept of a ΔE tracking detector was born. This detector is composed of two layers of plastic scintillators

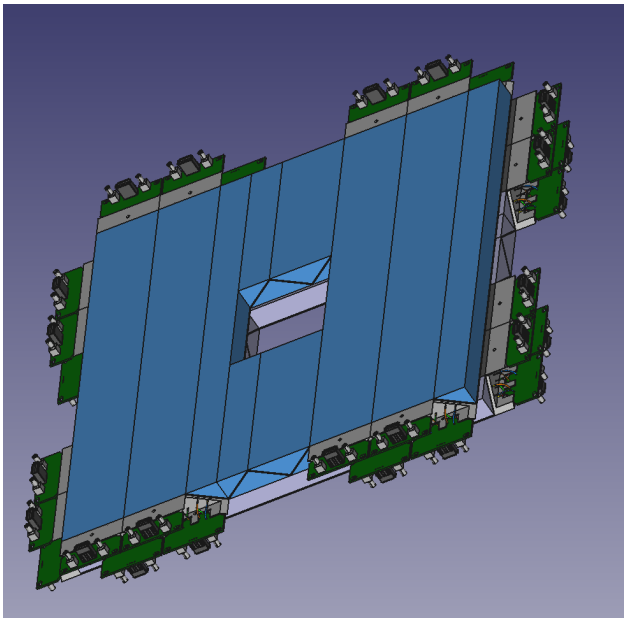

Figure 4.1: SiTH scheme

To fit around the beam pipe, the shorter bars will need to be trimmed to length. On each lateral face of the bars, custom designed pre-amplifier boards with a triangle cross section will be installed (see Figure 4.2). These boards have two independent op-amp powered channels, each of which can have two SiPM arrays. PM6660TP-SB0 6mm x 6mm SiPM arrays from Ketek were employed as sensors. One layer of Teflon for internal reflection enhancement is followed by a second layer of Tedlar foil for light tightness on the plastic scintillator bars. The pre-amplifier boards with the SiPMs will cover the faces of the bars, so they aren't covered. Between the pre-amplifier board and the SiPM arrays, a thin, white 3D-printed mask is sandwiched, allowing them to sit flat in a reflective at surface. The SiPMs-equipped pre-amplifier is housed in an aluminium frame with a 3D-printed mount that allows the scintillator bars to be pressure-fit between them. A thin silicone pad serves as

an optical contact between the SiPM arrays and the triangular bars, as well as preventing the plastic scintillators from falling out of the frame. A LEMO connector is used to feed the amplified SiPM signal from each channel out of the pre-amplifier, while a common voltage supply rail is attached on either side of the frame, allowing each pre-amplifier to be plugged in to give the required dual supply voltage. Two frames, each with three plastic scintillator bars, were placed and tested during the beam time of the 3rd iteration of the detector development (May 2018 [55]).

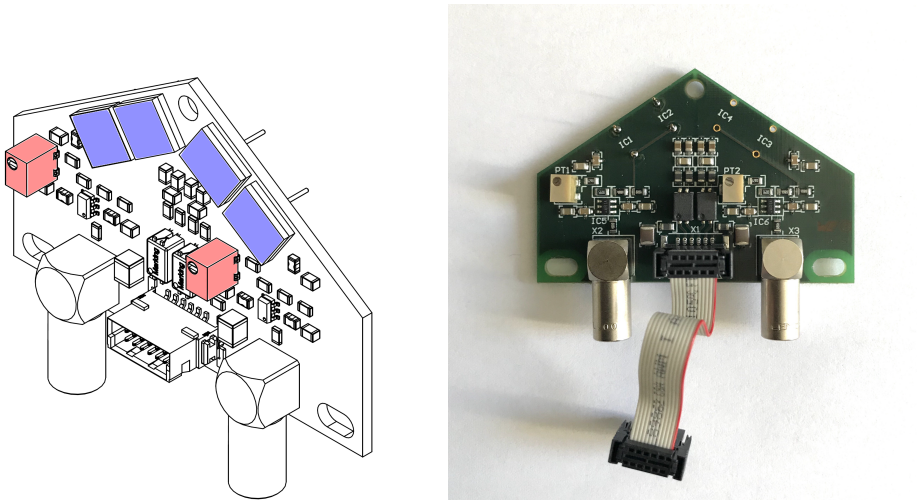

(a) Dual channel pre-amplifier model (b) Dual channel pre-amplifier picture

Figure 4.2: QS Electronics specifically created a dual channel pre-amplifier for the triangle E detector. Blue is used to represent the SiPM arrays. They are sketched on the front side of the PCB in this image, but they were later installed on the rear side so that they could contact the plastic scintillators. A red-coloured component is a potentiometer that allows each channel's gain to be adjusted individually, in order to optimise the avalanche region.

Reconstruction principle will be described in the following section (4.2).

4.1.1 Plastic Scintillators

Scintillators are materials that, once a charged particle passes through them, emit light in a small amount of time and with a number of photons proportional to the energy loss of the particle inside of the scintillating material.

As it passes, the incident particle gives part of its energy to the atoms and molecules of the scintillator causing, for example, the excitation in a higher energy level. When these de-excite they emit a photon of relatively low energy, typically in the visible or ultraviolet spectrum. This light pulse is then detected and amplified by suitable sensors, such as photo-multipliers.

Depending on the emission time one can observe *fluorescence*, when re-emission time is of the order of 10^{-8}s (that is of atomic transmission), or *phosphorescence* if the excited state is meta-stable, and the re-emission is delayed to a time ranging from μs to hours.

Both phenomena have an exponential trend and coexist in the scintillation mechanism, the simplest way, therefore, to describe the scintillator signal is the following:

$$N(t) = Ae^{-\frac{t}{\tau_f}} + Be^{-\frac{t}{\tau_s}} \tag{4.1}$$

where $N(t)$ is the number of photons emitted at time t, while τ_f and τ_s are the decay constants of the fluorescent (fast) and phosphorescent (slow) components. Constants A and B vary for different materials. As you can see in Figure 4.3 the fast component is the dominant one [74].

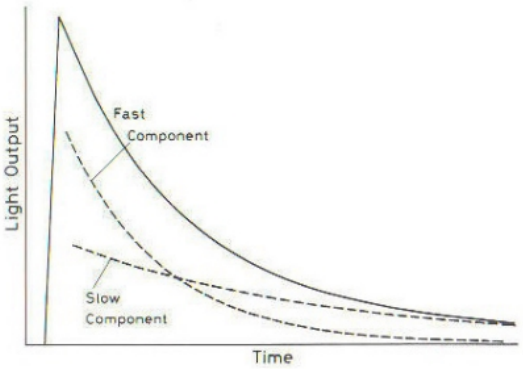

Figure 4.3: Representation of the exponential trend of the light emission of a scintillator in its two components and their sum.

A good scintillating detector has some characteristic properties:

- Ability to convert the kinetic energy of the particle into detectable light of energy proportional to that of the incoming particle,
- Fast response time, *i.e.* a low dead time, which is the interval in which it is not able to process small events,

- High conversion efficiency (from excitation energy into fluorescence radiation),
- Transparency to fluorescence radiation,
- Spectral zone compatible with the photo-multiplier response,
- Small decay constant τ_D, since the number of photons emitted at instant t goes as $N(t) = \frac{N_0}{\tau_D} e^{-\frac{t}{\tau_D}}$.

For SiTH's tracking bar EJ-200 plastic scintillator was chosen (see Tab. 4.1) [75]. The decision of this kind of scintillator was driven firstly by its wavelength of emission ($\sim$ 425 nm) that matches with SiPMs. It is a fast scintillator (rise time 0.9 ns and decay time of 2.1 ns), that makes it really suitable for this kind of detector. Considering that this scintillator was developed for general purpose and that it is very common, it made the detector affordable from the economic point of view.

Plastic scintillator model	EJ-200
Light Output [%Anthracene]	64
Rise Time [ns]	0.9
Decay Time [ns]	2.1
Pulse Width FWHM [ns]	$\sim$ 2.5
Wavelength of Max. Emission[nm]	425
Light Attenuation Length [cm] *	380

Table 4.1: Overview of the EJ-200 plastic scintillator principal characteristics.
*The typical 1/e attenuation length of a 1x20x200cm cast sheet with edges polished as measured with a bi-alkali photo-multiplier tube coupled to one end.

4.1.2 SiPM

As already described in JEPO subsection 3.1.2 Silicon Photon Multiplier are coupled with the EJ-200 plastic bar in order to convert the light to a signal. The SiPMs employed in the Beam Test of 2018 were PM6660TP-SB0 6mm x 6mm from Ketek which characteristics can be seen in Tab 4.2 [73] .

Unluckily the Ketek dismissed the production of that sensor before they were all acquired, so a new set of SiPMs has to be chosen and tested. Moreover

Sensor model	PM6660TP-SB0
Bias voltage range [V]	26.6 - 33.2
Spectral range [mm]	300 - 900
Peak sensitivity [nm]	430
Pixel size [μm]	60
Pixel per SiPM	$\sim$ 6600
SiPM fill-factor [%]	$\sim$ 66
SiPM area [mm^2]	6^2
SiPMs per array	single SiPM
Connector	2x single pin

Table 4.2: Overview of the PM6660TP-SB0 SiPM principal characteristics

the first SiPM support for PM6660TP-SB0 would not fit in the future design of the detector, so this change was forced (see Fig.4.4, previous PCB scheme is shown in 4.2).

New PCB design

As previous stated the PCB that was employed during the Test Beam of 2018 would not fit in the mechanical support of the detector. So it was moved out the readout from the SiPMs facing the surface of the scintillator. This will give enough space into the support.

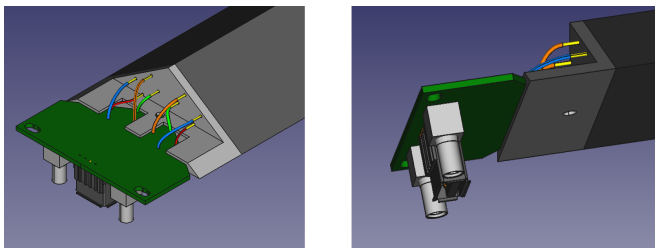

Figure 4.4: New PCB placement

4.2 Reconstruction principle

To obtain the **ΔE information**, the main information for the particle identification, the energy loss for each event in all the modules can be summed, so all the bars act as one solid layer of scintillator.

Position can be extracted from each bar's individual energy loss (see Fig. 4.5 for the simplified parallel configuration scheme). The amount of energy that is deposited in one scintillator is due to the position where the particle passes thought the scintillator, and so the triangular cross section of the SiTH modules allow to get the incident position y depending from the effective path length x_1 and x_2 into the scintillators.

The energy deposit is proportional to this distance as in the Bethe-Bloch formula. The energy loss in plastic scintillator material is rather small, and its value can be approximated as a linear function of the path:

$$\Delta E_n(x) \approx K_n \cdot x_n, \tag{4.2}$$

where K describes the energy loss per distance and the index n stands for the module. Assuming that the energy loss in the first module is small compared to the total kinetic energy of the particle one can assume that the energy loss per unit length K_n is constant for both modules, *i.e.* $K_1 \approx K_2$. Considering this assumption, the following ratio equation can be written from Eq.4.2:

$$\eta = \frac{\Delta E_1 - \Delta E_2}{\Delta E_1 + \Delta E_2} \tag{4.3}$$

Simplified parallel configuration algorithm

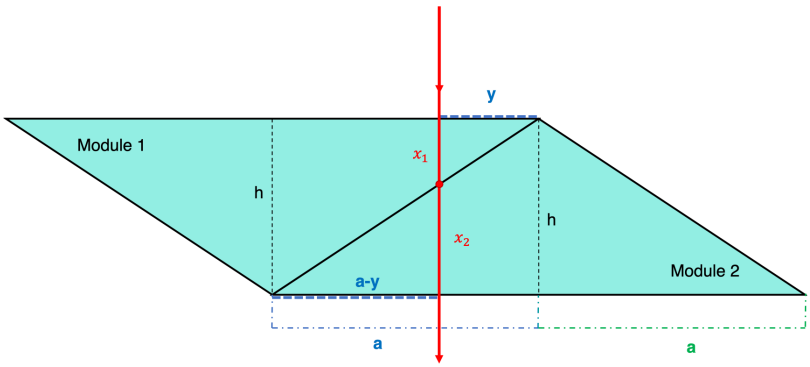

Figure 4.5: Schematic of two ΔE SiTH modules to discuss the geometrical consideration needed for the calculation of the position reconstruction. Considering a particle (red line) hitting the first module at the incident position y and travelling a distance of x_1 in Module 1 before it enters Module 2 and travels a distance of x_2.

From the triangle of scheme in Fig.4.5, the following geometrical relation can be obtained using intersecting lines theorem:

$$\begin{aligned} \frac{y}{x_1} = \frac{a}{h} \rightarrow x_1 = \frac{h}{a} \cdot y, \\ \frac{a-y}{x_2} = \frac{a}{h} \rightarrow x_2 = \frac{h}{a} \cdot (a-y), \\ \Updownarrow \\ \eta = \frac{x_1 - x_2}{x_1 + x_2} = y \cdot \frac{2}{a} - 1. \end{aligned} \tag{4.4}$$

Combining the last two equations (Eq.4.3 and Eq.4.4) the incident position y formula can be extracted:

$$y = \frac{a}{2} \cdot (\eta - 1) = \frac{a}{2} \cdot \Big(\frac{\Delta E_1 - \Delta E_2}{\Delta E_1 + \Delta E_2} + 1 \Big). \tag{4.5}$$

Therefore the incident position of a particle can be reconstructed from the deposited energy in two stacked triangular bars. The position using this method is given relative to the tip of the lower module (2), but since the modules absolute position is known, the absolute position of the particle can be easily calculated as well.

Two perpendicular layers of triangular modules allow to get x and y positions.

General SiTH algorithm

The "Simplified parallel" algorithm works with the assumption that the particle track incidents almost perpendicularly to the base of the module. This however is not true in a general case while using many modules. Fig.4.6a shows explicitly such a case where the particle incidents obliquely to the module.

Let's consider a beam travelling along $\widehat{k}$ (the z axis), and a layer of n tracker modules oriented to measure position in the $\widehat{s}$ direction perpendicular to $\widehat{k}$. A particle passes through modules q and r and deposits energies E_q and E_r (indexed according to the scheme shown in Fig.4.6b). Considering the target

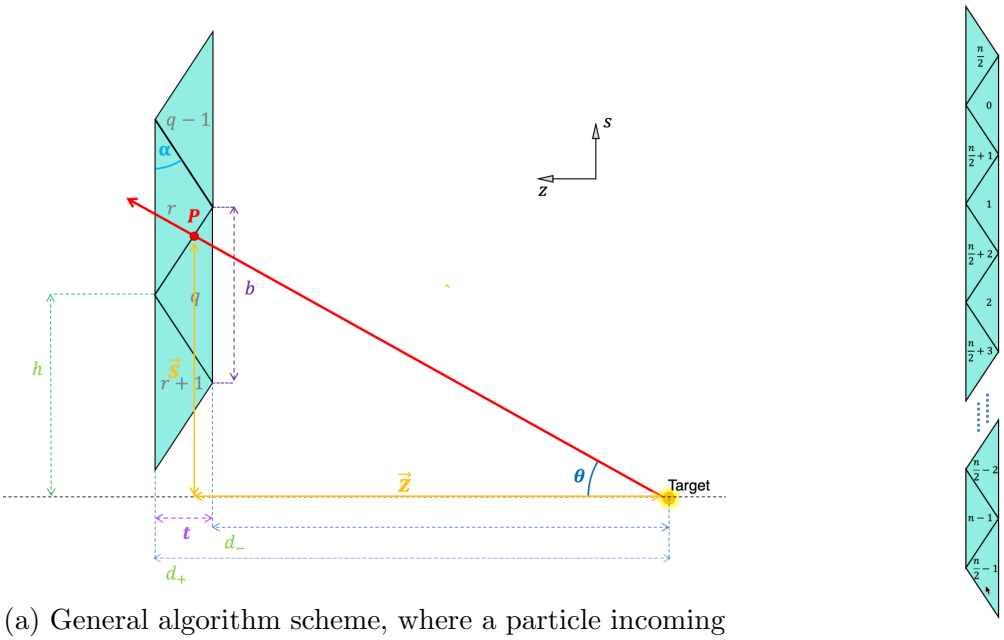

(a) General algorithm scheme, where a particle incoming from the target hits the q and r SiTH modules. The point P indicates the place where the impinging line crosses the two modules, and its components are calculable with the Equation 4.7.

(b) SiTH indexing scheme

Figure 4.6: General SiTH algorithm and its indexing scheme are presented.

position as the origin, and recalling that

$$\eta\left(q,r\right)=\frac{E_q-E_r}{E_q+E_r}, \tag{4.6}$$

the s-component of the point P, where the particle hits the interface between two modules, will be given by:

$$\vec{s}=\frac{b}{4}[n-4q-3-(-1)^{\varepsilon}(1-\eta)]\,\widehat{s}, \tag{4.7a}$$

where $\varepsilon=r-q+\frac{n}{2}+1$.
Its z-component will be:

$$\vec{z}=d_{-}+\frac{t}{2}(1+\eta)\,\widehat{k}. \tag{4.7b}$$

Here b is the base and t is the thickness of each triangular module, d_{-} is the distance between the source and the first surface of the layer.

$\vec{s}$ can be $\vec{x}$ or $\vec{y}$, depending on the orientation of the module. In the case of SiTH detector, Front layer is x-oriented while Back layer is y-oriented. Therefore the position vector $\vec{r}$ of the point of incidence of the particle at the surface of the LYSO modules would be given by Eq.4.8.

$$\vec{r} = \frac{l}{z_B}\vec{x} + \frac{l}{z_F}\vec{y} + l\,\hat{k}. \tag{4.8}$$

where l is the distance between the source and the LYSOs, z_F and z_B are the measurements of $\vec{z}$ made by the Front and the Back layers.

4.3 Test Beam 2018

During the Test Beam of 2018 an experiment was performed in order to find the *least-count* of the SiTH modules. Therefore, two layers of triangular bars with three modules each, were set up parallel to one another as shown in Fig.4.7. This Figure depicts the measuring process used with the 3rd detector development configuration during the May 2018 beam time. The first frame, which had three scintillator bars, was fixed to the beam pipe's exit window and positioned so that the beam would pass through the scintillators between the first (F_01) and second (F_03) modules. As can be seen in the left two-dimensional histogram of Figure 4.8, the energy deposited in these two modules was plotted against each other in a ΔE vs. ΔE spectrum. Even though the frames carrying the scintillator bars were relocated as close to the exit window as possible, the 270 MeV deuteron beam employed for this test showed some angular dispersion.

From the Front and Back layers, values of η_F and η_B are obtained from Eq. 4.3. The difference between this values, defined as $offset$, would be proportional to the difference in position of the two layers. Therefore, the resolution of the $offset$ measurement at each step would indicate the *least-count* of the detector. Then the code can recognise the peaks of the $offset$ measurements and then can fit them with different Gaussian functions to extract the resolution of the detector (*e.g.* Fig.4.9).

4.3.1 Event acquisition

The signal is selected inside *event number* parameter of DAQ tree (in order to put the same event tracks together). Inside this number the events coming

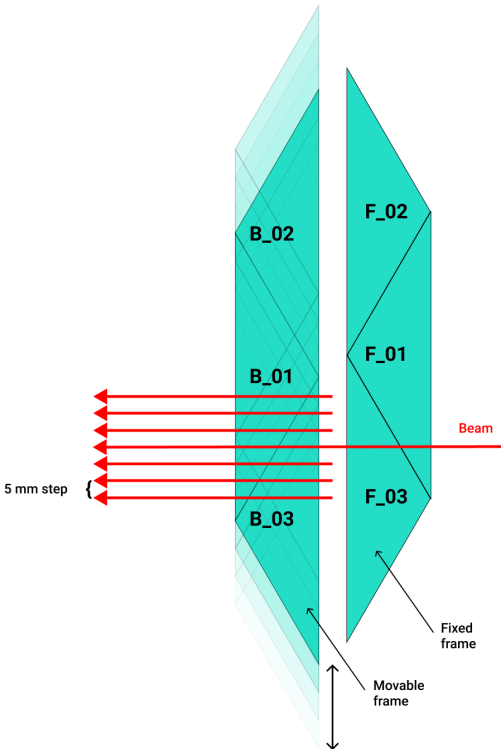

Figure 4.7: The measuring process used to test the position reconstruction utilising triangle ΔE detectors is depicted schematically in this diagram. In the beam path, two frames with three scintillator bars each were placed. The first frame (modules labelled with **F**) was attached to the beam pipe and could not be moved vertically, whereas the second frame (modules labelled with **B**) was attached to the experimental table and could be moved vertically. With a vertical spacing of 5 mm, the second frame was moved to six distinct positions.

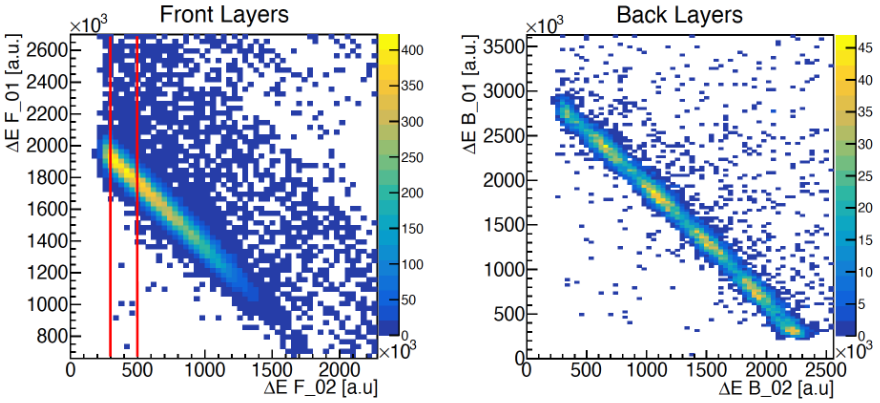

Figure 4.8: (a) shows ΔE vs. ΔE spectra in module F_01 and F_02 for the first, fixed layer. The same spectra, for the second movable layer, with the modules B_01 and B_02 is shown in (b). The first layer narrowed the beam by acting as a filter. In (b) spectrum, only events that fell within the cut range (marked in red) in (a) spectrum were evaluated. The measurements taken at the six various vertical positions, which are represented by the distinct spots in the band, can be observed in plot (b). [55]

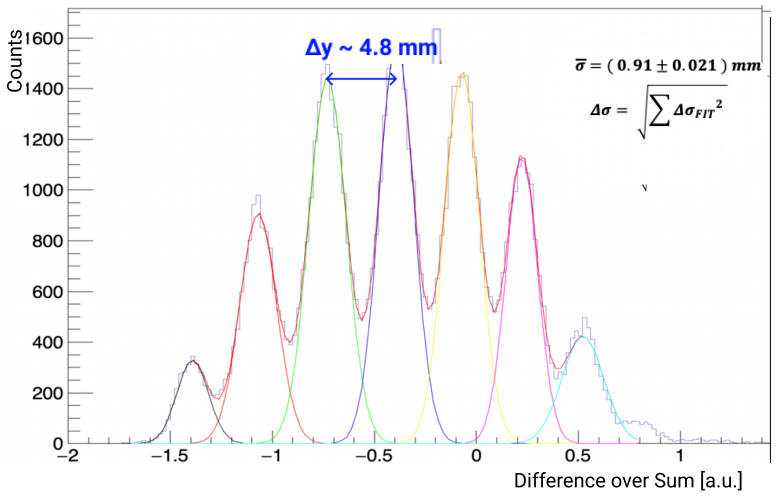

Figure 4.9: *offset* histogram of Test Beam, with the scan performed over one direction moving the back layer (see Fig.4.7), using colours to highlight different step of the scan. Resolution and average peak distance is also reported.

from the tracking module that we want to analyse are selected (*e.g.* F_01). The event is considered *valid* if every SiPM of the module gives a signal, this means that there is enough photons to trigger all the photo-multipliers. A schematic view of this process is given in Fig. 4.10.

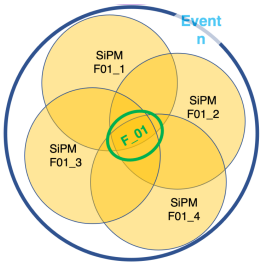

Figure 4.10: Signal selection scheme. In this case inside the event n, the selected module was F_01 with all SiPMs triggered.

The module signal can be now used as energy to perform the position reconstruction. The modules' signals can be compared in 2D histogram, cutting the front layer energy the beam can be sliced and bumps of the scan can be seen in the back modules (see Fig. 4.8)

4.3.2 Results

The resolution obtained from the Test Beam of 2018, averaging all the Gaussian fits σs is:

$$\sigma_{ave} = (0.907 \pm 0.003)\,\text{mm}.$$

The error is calculated as the summation in quadrature of the Gaussian sigma errors:

$$\Delta\sigma = \sqrt{\sum \Delta\sigma_{FIT}^2}.$$

Here, the relation in Equation 4.5 was used to transform *offset-units* into mm. While the distance between peaks, calculated considering the X position of the Gaussians' peaks and then averaged is $\Delta x \approx 4.78$ mm. This means that the Δx steps of the test beam were not exactly 5 mm

This results updates the previous ones from Müller that found a σ of 1.46 mm during the first analysis of the data [55] (See Fig. 4.11).

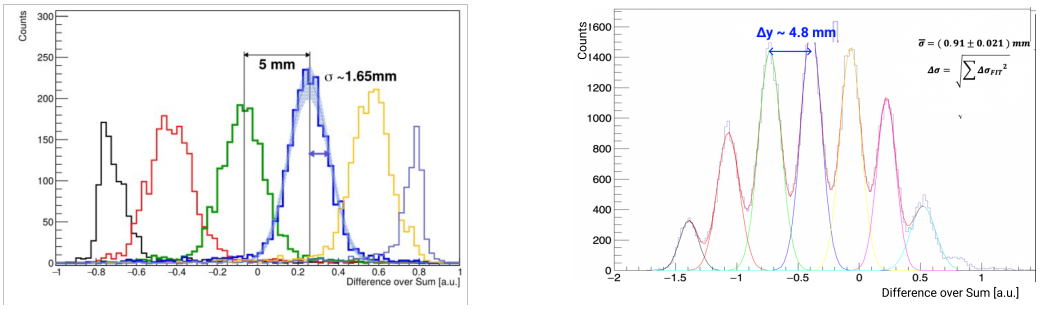

(a) Müller's result of 2019 [55]

(b) Results of this work

Figure 4.11: Comparison between Müller's 2019 result and the work of this thesis on the same data set. In the first case data for each step was processed directly from DAQ, that allowed the discrimination of the step events and subsequent scaling over the maximum. On the right this was not possible, since all the data were all mixed up so a multi-Gaussian function was considered for the fitting. Here the individual peaks from the fit are highlighted.

The found SiTH linear resolution is about 0.9 mm, due to the fact that the LYSO matrix provides a resolution of 1 cm (from crystal dimension of 3 cm) the installation of this detector could increase the spatial resolution by about

one order of magnitude.

$$\sigma_{LYSO} = \frac{3\text{cm}}{\sqrt{12}} \sim 1\text{cm}. \tag{4.9}$$

4.4 Geant4 Simulation

A Geant4 simulation was planned to evaluate the performances of the whole SiTH. First it was simulated the 2018 Test Beam configuration to get the same result then exploit those parameters in the final simulation.

G4 uses plastic scintillator characteristics from the ELJEN TECHNOLOGY data sheet [75]:

Ratio H:C Atoms	1.104
Density [g/cc]	1.023

Each module is shaped from the extrusion of an isosceles triangle, with base length of 6 cm and a height of 2 cm, coated with Teflon,Tedlar and aluminium as for the prototype one. Each module was then oriented in order to match the proper configuration.

At the moment there is no optical generation/absorption simulated, the energy of the module is acquired from the Geant4 physical volume.

4.4.1 Test-Beam Like configuration (Parallel)

In this configuration (see Fig.4.12)the aim was to simulate the 2018 Test Beam tuning the *Detector Energy resolution* (dE) parameter in order to match Müller's and section 4.3 results.

Detector energy resolution scan and residuals

As previously stated the main parameter to get from the simulation is the *detector energy resolution*, that indicates how much the SiTH detector smears the energy that enters in it. When the $offset$ plot obtained by the simulation scan was overlaid on the one from the Test Beam, there was a misalignment, as can be seen in Fig. 4.13. This was postulated to be due to a machine error in the translation of the back layer during the Test Beam.

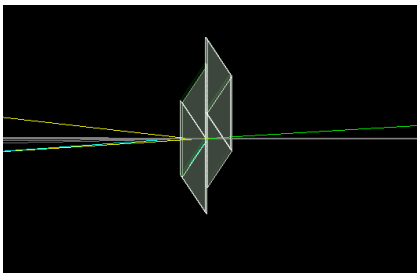

(a) TB like configuration side view

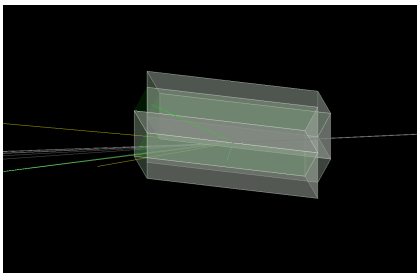

(b) TB like configuration front view

Figure 4.12: TB Like configuration

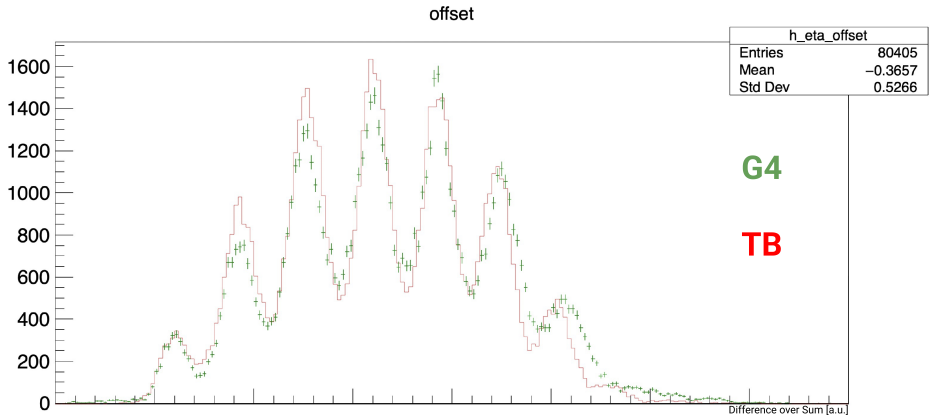

Figure 4.13: The superimposing of *offset* parameter for TB2018 and G4 simulation is shown, scaled over the entries in order to match. In red Test Beam data in green the Geant4 results are indicated,. It is clear also from here that the peaks are not aligned, it means that the Δx steps of the test beam were not exactly 5 mm

To test this hypothesis the peak positions relative to the Front layer were extracted from the Test Beam and transformed into "real distance" using the relation from the Equation 4.5. These distances would be the true positions of the Back layer at the various steps. Applying this correction to the Back layer translations in the simulation, a better alignment between the $offset$ plots of Test Beam and simulation was obtained, as shown in Fig. 4.14.

In order to obtain the proper dE parameter a scan was performed and linear fit over the residuals was analysed, the goal for the parameter intercept of the fit is expected to be 1, since the residual is a ratio and the aim is to have

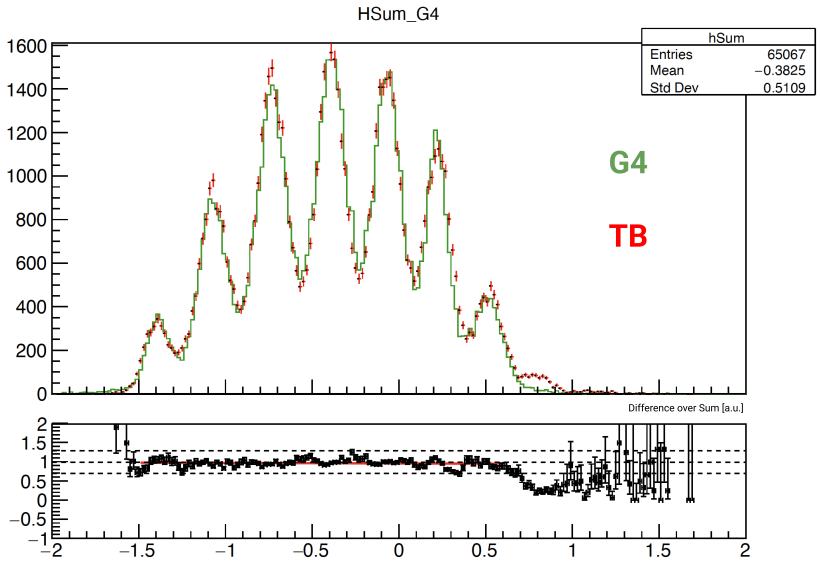

Figure 4.14: The superimposing of *offset* parameter for TB2018 and G4 simulation is shown, scaled over the event recorded at each step. In red Test Beam data and in green the Geant4 results are indicated. The resolution width is comparable with the previous one and the peaks are quite well described. Below, residual plot (G4/TB) is shown, in which a linear fit is applied.

the same plot, while the slope is expected to be 0 since the ratio should be flat.

A χ^2 minimizer was used to select the optimum energy smearing that most resembles the real detector energy resolution. The selected value for dE is 0.22. In Fig. 4.14 the result for $dE = 22\%$ is shown.

Results

Applying the proper dE the seven-Gaussian fit result for Geant4 simulations in *parallel configuration* gives:

$$\sigma_{ave} = (0.911 \pm 0.003)\,\text{mm}.$$

The error is calculated as the summation in quadrature of the Gaussian sigma errors:

$$\Delta\sigma = \sqrt{\sum \Delta\sigma^2_{FIT}}.$$

This result matches with real data of the test beam when the value of the *detector energy resolution* $dE = 0.22$, so this value has been exploited for the whole SiTH simulation.

4.4.2 Final SiTH configuration (Perpendicular)

With the proper dE setting the final SiTH configuration can be applied in the simulation. It consists of two perpendicular layers with 14 modules each, as can be seen in Fig. 4.15.

From the position $\vec{r}$ of the projected incidence at the LYSO modules (Eq. 4.8) the angular behaviour can be extracted as follows:

$$\begin{aligned} \theta &= \operatorname{atan}\left(\sqrt{x^2 + y^2}/d\right) \\ \phi &= \operatorname{atan}2(y, x) \end{aligned} \tag{4.10}$$

where d is the distance of the target (origin) from the first surface of the LYSOs.

In order to estimate angular behaviour the whole detector, two scans were performed in this configuration, along the polar and the azimuthal directions (θ and ϕ). ϕ has been scanned with steps of 22.5 °, while θ with 2 ° step starting from 5 ° to avoid the inner hole (see Fig. 4.15). Test simulations of these scans (with fewer iterations) are shown in Fig. 4.16

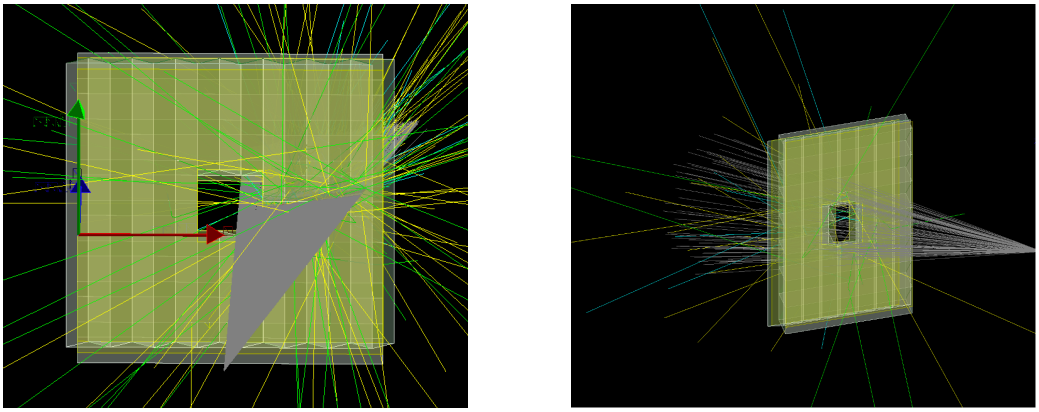

(a) ϕ scan visualisation (b) θ scan visualisation

Figure 4.15: Angular scan visualisation

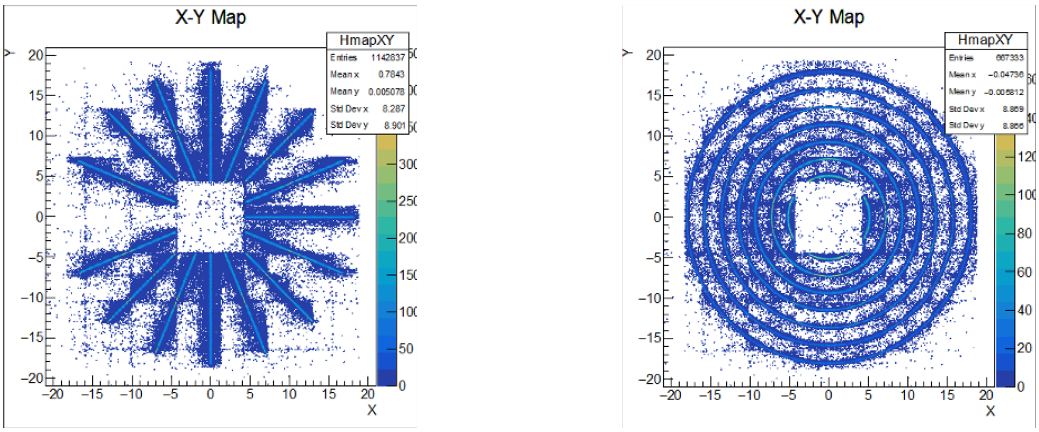

(a) Detector X-Y map for ϕ-scan (b) Detector X-Y map for θ-scan

Figure 4.16: Examples of the schemes of ϕ and θ scans as acquired by the detector and reconstructed using the methods described in Sec. 4.2

Results

Resulting plots of the scan described before are shown in the Figures 4.17 and 4.18.

The behaviour of the resolution over the range of angles during the scan is shown in Fig.4.19.

Since from the configuration of the spherical coordinates system, the expression for ϕ resolution depends on θ, which is the polar angle of incidence at the LYSO modules, for the ϕ scan a specific value of θ was selected for fitting such that radial distance of the particle incidence (r_0) from the centre was 12 centimetres. This distance was chosen such that all the particles incident on the detector. Therefore the ϕ resolution can be written as a function of θ:

$$\sigma_\phi(\theta) = r_0 \cdot \frac{\overline{\sigma_{\phi scan}}}{d} \cot\theta,$$

$\overline{\sigma_{\phi scan}}$ is the average values of the sigma from the Gaussian fits in ϕ scan and d is the LYSO distance from the target (66 cm)

The resulting average resolutions from the angular scans are:

$$\begin{aligned} \sigma_\phi &= [(0.057 \pm 0.007) \cot\theta]^\circ \\ \sigma_\theta &= (0.0912 \pm 0.0003)^\circ \\ \Delta\sigma &= \sqrt{\sum \Delta\sigma^2_{FIT}} \end{aligned} \tag{4.11}$$

The matrix of LYSOs provides a polar angular resolution around $\frac{2.5}{\sqrt{12}}^\circ$ (the angle subtended by the crystal width) and the found SiTH θ resolution is about 0.09 °.

This result is in agreement with improvement found for the linear resolution in Section 4.3.

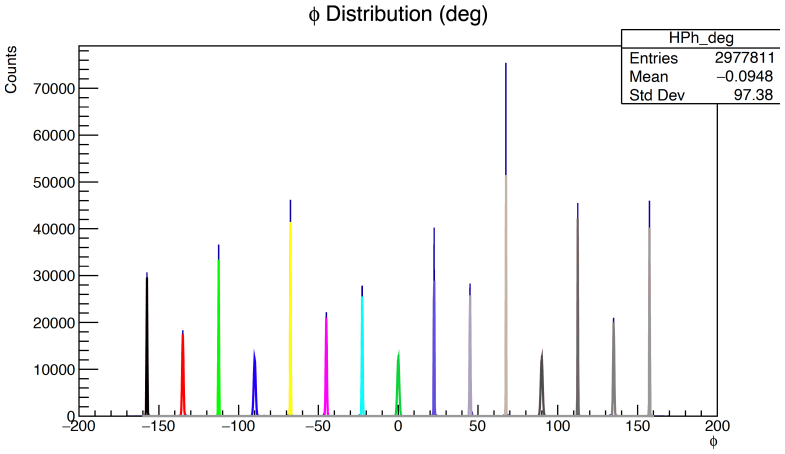

(a) ϕ scan distribution

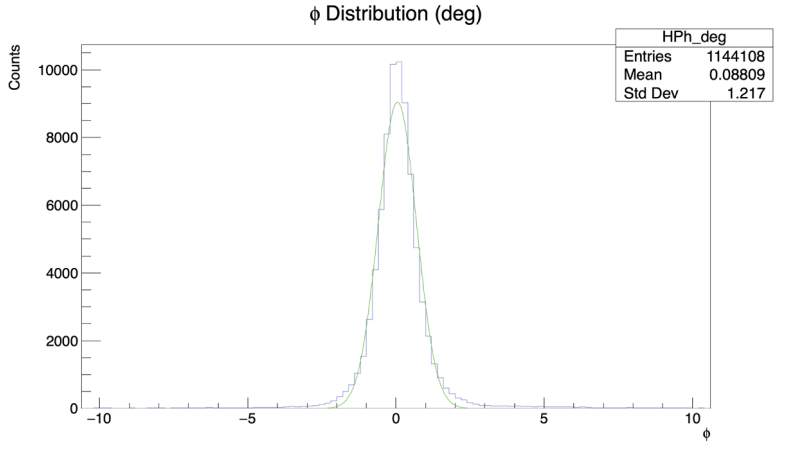

(b) ϕ scan distribution zoomed on one single point

Figure 4.17: ϕ scan distribution plots, fitted with a n-Gaussian fit over all the peaks, highlighted with different colours.

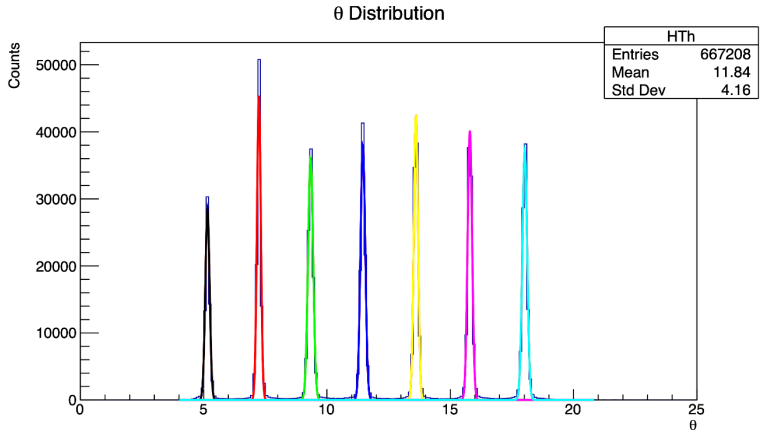

(a) θ scan distribution

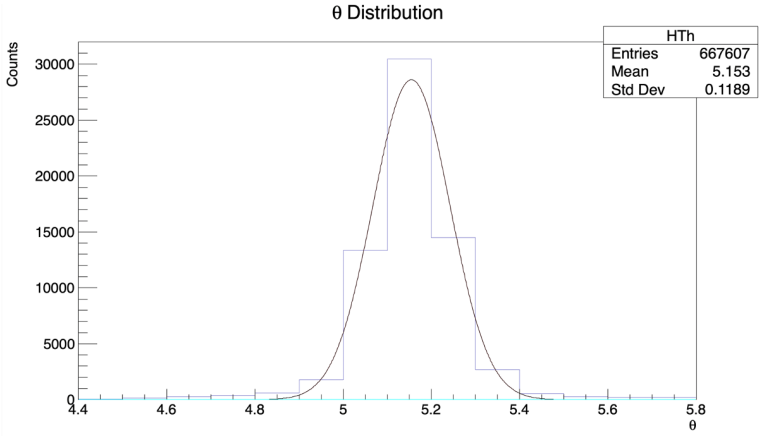

θ scan distribution zoomed on one single point

Figure 4.18: θ scan distribution plots, fitted with a n-Gaussian fit over all the peaks, highlighted with different colours.

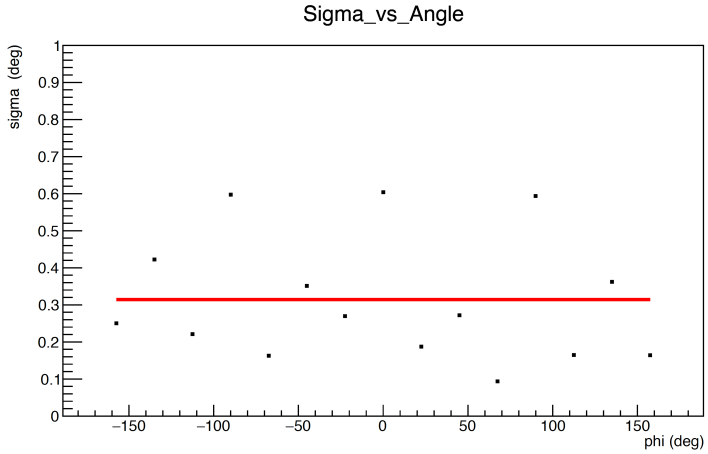

(a) σ vs ϕ distribution at $l \sin\theta = 12$ cm, that lies such that all the particles incident on the detector.

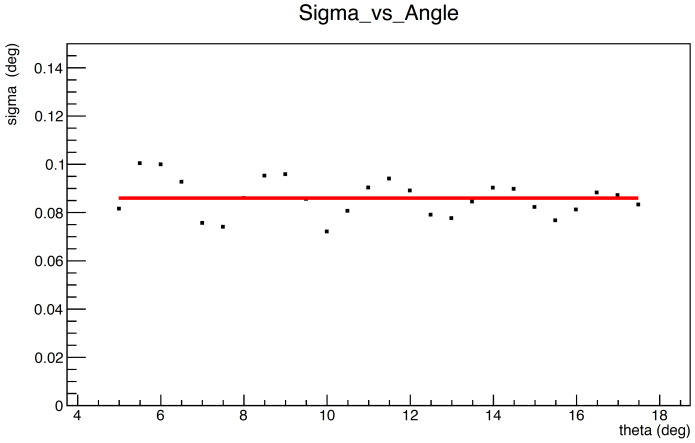

(b) σ vs θ distribution.

Figure 4.19: σ vs angle distribution. In (a) it is visible that diagonal lines have lower σ values since they incident upon more vertices and so there are calculated without errors in the reconstruction algorithm. While the orthogonal ones (-90°, 0° and 90°) incident on less vertexes and so it results in higher values of σ. In (b) the vertex interplay here is determined by special radii where more vertices are traversed. The overall convergence is due to the fact that in general circles with larger radii incident upon more vertices.

Chapter 5

Conclusions and outlook

The JEDI collaboration aims to directly measure the EDM of protons and deuterons in the accumulation ring. In order to detect an EDM we look for time development of the particle bunch polarisation, exploiting the energy deposit in LYSO crystal modules to identify the particles. Given that the expected EDM is very small, the precision of the polarimeter used is of utmost importance to the experiment.

The work of this thesis is focused on a possible upgrade for the existing polarimeter of the experiment, *i.e.* SiTH: a tracking hodoscope made of triangular plastic scintillator bars. The polarimeter LYSO modules have a very high precision when it comes to calorimetry, but not in particle tracking due to the limitation on its size. The idea is that the combination of the SiTH and LYSO modules can provide a high precision in both calorimetry and tracking reconstruction. Due to the unique geometry of the arrangement and the individual readout of the tracker bars, this hodoscope has been shown to be capable to track a particle on the polarimeter modules to within 0.9 mm.

A model of the tracker bar was constructed in the Geant4 simulation environment. This model was benchmarked by recreating the conditions of the 2018 Test Beam and comparing the results of the stimulated beam test with the real one.

The SiPM modules and the associated electronics can resolve energies deposited by the particles to within a certain error. This is called the *detector energy resolution* (dE). Since the Geant4 model does not simulate the SiPM modules directly, a smearing function was applied to simulate its effects on the acquired data. The standard deviation of this smearing function at which the simulated readout matches with the Test Beam data was earmarked for future simulations of SiPM behaviour.

Finally a model of the fully equipped SiTH was constructed in Geant4, and its performance with particle trajectory reconstruction was also estimated via simulated beam tests.

The following section summarizes the results obtained in the previous chapters and describes a brief outlook of the future activities.

5.1 Results

The resolution of the real SiTH tracker bars as obtained from the analysis of the data of the Test Beam of 2018 is:

$$\sigma = (0.907 \pm 0.003)\,\text{mm}.$$

This shows that when SiTH is combined with the calorimeter, its position resolution will improve by about one order of magnitude.

To benchmark the SiTH simulator in Geant4, a scan was performed in a configuration, which precisely recreate the material, geometrics and beam condition of the TB2018. The resolution of the simulated tracker bars obtained from this test is:

$$\sigma = (0.911 \pm 0.003)\,\text{mm}.$$

This result matches with real data of the test beam when the value of the *detector energy resolution* $dE = 0.22$, so this value has been exploited for the whole SiTH simulation.

The full SiTH detector was simulated and it's performances investigated with two angular scans, as described in Chapter 4. The results of these scans are shown in the Figure 5.2.

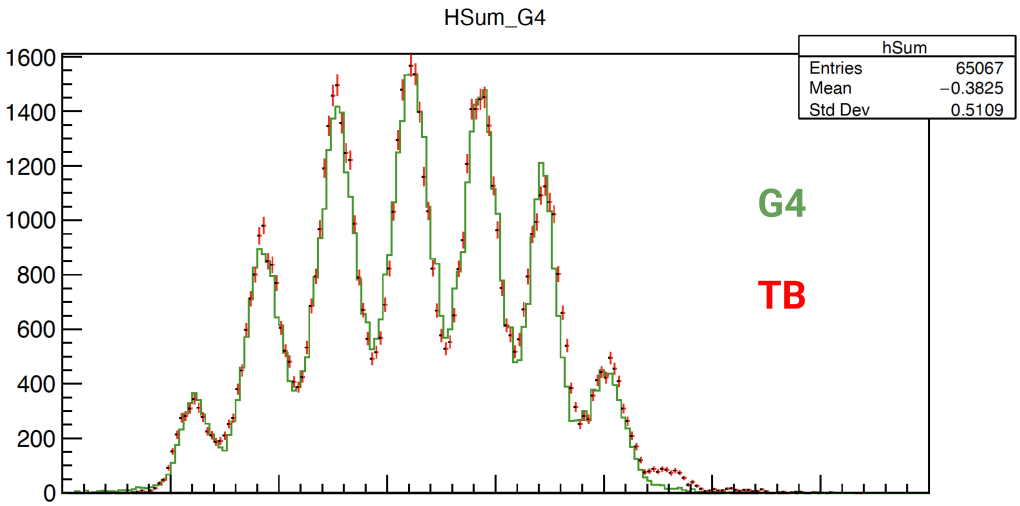

Figure 5.1: The superimposing of *offset* parameter for TB2018 and G4 simulation is shown, scaled over the event recorded at each step. In red Test Beam data and in green the Geant4 results are indicated.

The resulting average resolutions from the angular scans are:

$$\sigma_\phi = [(0.057 \pm 0.007)\cot\theta]^\circ$$
$$\sigma_\theta = (0.0912 \pm 0.0003)^\circ$$

The LYSO matrix causes a polar angular resolution of $\sim \frac{2.5}{\sqrt{12}}^\circ$. The found results of SiTH provides an improvement of the existent resolution by about one order of magnitude, an improvement in agreement with the linear resolution's one.

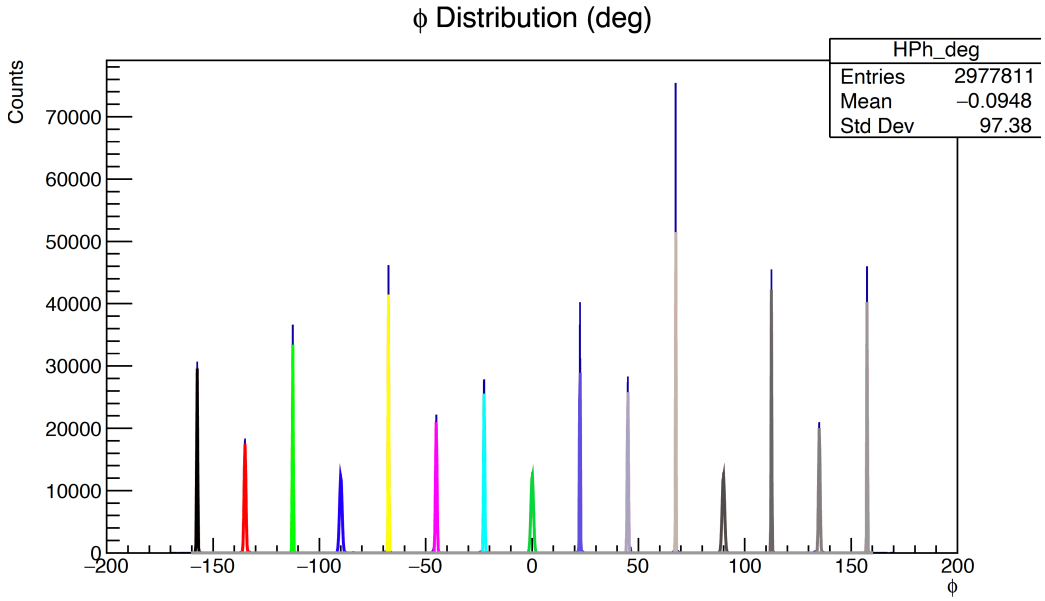

(a) ϕ scan distribution

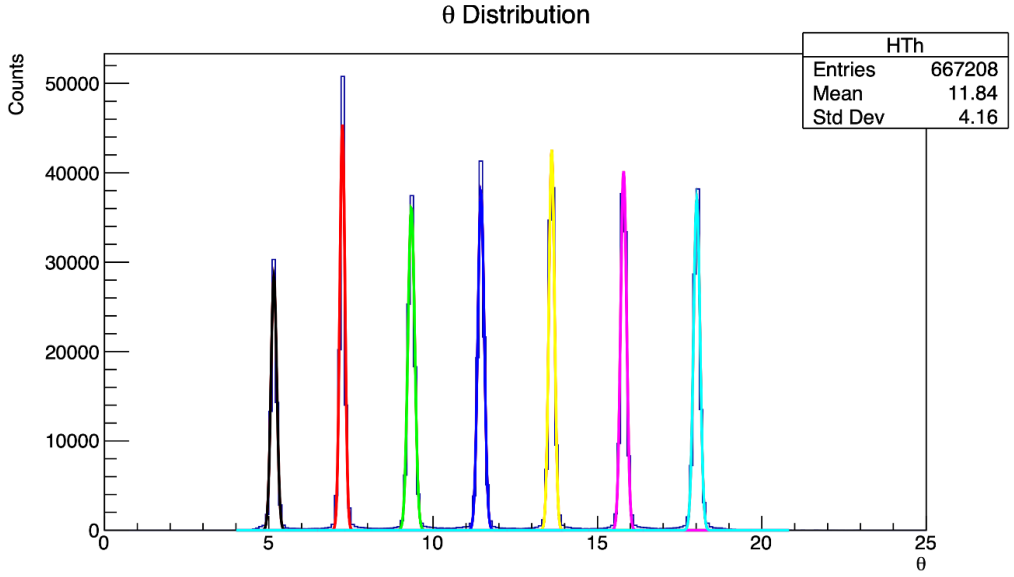

(b) θ scan distribution

Figure 5.2: $\phi - \theta$ scan distribution plots, fitted with a n-Gaussian fit over all the peaks, highlighted with different colours.

5.2 Outlook

The main achievement of this work is to have developed a working Geant4 simulation of the SiTH detector that can be implemented into the existing JEPO simulator. In addition to this, an analysis framework was developed that reconstructs the trajectory of the particle and provides a precise position of incidence on the LYSO calorimeters. This implementation can be used to investigate the improvements that this kind of tracker will make to the final polarimeter.

Once the improvements are asserted, the assembling of the remaining SiTH modules can resume and, finally, the installation of the hodoscope to the JEPO detector can be done.

As stated, the time development of vertical spin is fundamental to detect an EDM. Since in COSY there currently exist technical limitations on the spin coherence time and overall beam-time, the expected magnitude of polarisation build-up due to intrinsic EDMs is very small. It is due to this that precise particle tracking is very essential to measuring this polarisation build-up.

Most of the links in the bibliography are `hyperlinks`. I would suggest not copying and paste,but click on them instead.

Bibliography

[1] `JEDI_collaboration_homepage`

[2] **Matter and Antimatter in the Universe**.
L.Canetti, M.Drewes, and M.Shaposhnikov.
New Journal of Physics, 14 (Apr.2012).
`DOI:10.1088/1367-2630/14/9/095012.`

[3] **Recent Progress In Baryogenesis**
A.Riotto and M.Trodden
Annual Review of Nuclear and Particle Science, 49, (Jan.1999)
`DOI:10.1146/annurev.nucl.49.1.35.`

[4] $\mathcal{CP}$ **violation and baryogenesis**
W.Bernreuther. Lect.Notes Phys., 591 (2002), pp.237-293.
`DOI:10.1088/0067-0049/192/2/18.`

[5] **Seven-Year Wilinson Microwave Anisotropy Probe- (WMAP) Observations: Cosmological Interpretation**
E.Komatsu et al.
The Astrophysical Journal Supplement Series, 192.2 (2011).
`DOI:10.1088/0067-0049/192/2/18`

[6] **Violation of $\mathcal{CP}$ Invariance, C asymmetry, and baryon asymmetry of the universe**
A.D.Sakharov.
Pisma Zh.Eksp.Teor.Fiz., 5 (1967), pp.32-35.
`DOI:10.1070/PU1991v034n05ABEH002497`

[7] **Modern quantum mechanics**
J.J.Sakurai.
Addison-Wesley Publishing Company (1994).

[8] **Question of Parity Conservation in Weak Interactions**
T.D.Lee, C.N.Yang ùù Phys.Rev.104, 254 (1956)
DOI:10.1103/PhysRev.104.254

[9] **Experimental Test of Parity Conservation in Beta Decay**
C.S.Wu, E.Ambler, R.W.Hayward, D.D.Hoppes, R.P.Hudson
Phys.Rev.105, 1413 (1957)
DOI:10.1103/PhysRev.105.1413

[10] **Helicity of Neutrinos**
M.Goldhaber, L.Grodzins and A.W.Sunyar
Phys. Rev. 109, 1015 (1958)
DOI:10.1103/PhysRev.109.1015

[11] **Discrete symmetries and $\mathcal{CP}$ violation: from experiment to theory**
M.S.Sozzi
Oxford Graduate Texts.Oxford Univ.Press (2008)
DOI:10.1093/acprof:oso/9780199296668.001.0001

[12] **Field Quantization**
W.Greiner and J.Reinhardt
Springer-Verlag Berlin Heidelberg (1996)

[13] **Introduction to Quantum Mechanics**
D.J.Griffiths
Pearson Publishing Company (1995).

[14] **First direct observation of time-reversal non-invariance in the neutral-kaon system**
A.Angelopoulos et al.
Physics Letters B Volume 444, 1–2, (1998) pp. 43-51
DOI:10.1016/S0370-2693(98)01356-2

[15] **Evidence for the 2π Decay of the K_2^0 Meson**
J.H.Christenson, J.W.Cronin, V.L.Fitch and R.Turlay
Phys. Rev. Lett. 13, pp. 138-140 (1964)
DOI:10.1103/PhysRevLett.13.138

[16] **Behavior of Neutral Particles under Charge Conjugation**
M.Gell-Mann and A.Pais
Phys. Rev. 97, 1387-1389 (1955)
DOI:10.1103/PhysRev.97.1387

[17] **Extensive Optimization of a Simulation Model for the Electric Dipole Moment Measurement at the Cooler Synchrotron COSY**
V.Poncza
RWTH Aachen University (2021)
Thesis_Poncza.pdf

[18] **Searches for new physics with free neutrons and radioactive atomic nuclei**
N.Severijns
Europhysics News 52 (4) 22-25 (2021)
DOI:10.1051/epn/2021405

[19] **Experimental Limit to the Electric Dipole Moment of the Neutron**
J.H.Smith, E.M.Purcell, and N.F.Ramsey
Phys.Rev.108, pp.120-122 (1957)
DOI:10.1103/PhysRev.108.120

[20] **Schiff Moment of the Mercury Nucleus and the Proton Dipole Moment**
V.F.Dmitriev, R.A.Sen'kov
Phys. Rev. Lett. 91, 212303 (2003)
DOI:10.1103/PhysRevLett.91.212303

[21] **Precursor experiments to search for permanent electric dipole moments of protons and deuterons at COSY**
F.Rathmann, N.Nikolaev
Proceedings of 8^{th} International Conference on Nuclear Physics at Storage Rings (2012)
DOI:10.22323/1.150.0029

[22] **AGS Proposal : Search for a permanent electric dipole moment of the deuteron nucleus at the $10^{-29}\,e$ cm level**
D.Anastassopoulos, L.Anastassopoulos et al.
(2008)
AGS_Proposal.pdf

[23] **Revised experimental upper limit on the electric dipole moment of the neutron**
J.M.Pendlebury et al.
Phys. Rev. D 92, 092003 (2015)
DOI:10.1103/PhysRevD.92.092003

[24] **Improved limit on the muon electric dipole moment**
G.W.Bennett et al.*(Muon (g-2) Collaboration*)
Phys.Rev.D 80, 052008 (2009)
DOI:10.1103/PhysRevD.80.052008

[25] **Order of Magnitude Smaller Limit on the Electric Dipole Moment of the Electron**
J.Baron et al. *ACME collaboration*
Science Vol. 343,6168 (2014)
DOI:10.1126/science.1248213

[26] **Improved Limit on the Permanent Electric Dipole Moment of ^{199}Hg**
W.C.Griffith et al.
Phys. Rev. Lett. 102, 101601 (2009)
DOI:10.1103/PhysRevLett.102.101601

[27] **The search for electric dipole moments of charged particles using storage rings**
V.Shmakova
Talk at 16^{th} International Workshop on Meson Physics (2021) - slide 5
Shmakova_Meson_2021.pdf

[28] **New Method of Measuring Electric Dipole Moments in Storage Rings**
F.J.M.Farley et al.
Phys. Rev. Lett. 93, 052001 (2004)
DOI:10.1103/PhysRevLett.93.052001

[29] **nEDM experiment at PSI: Data-taking strategy and sensitivity of the dataset**
C.Abel et al.
EPJ Web Conf. 219 (2019)
DOI:10.1051/epjconf/201921902001

[30] **ERC Advanced Grant 2019 Research proposal [Part B1] Axion Storage Ring Experiments**
J.Pretz
Asterix_ERC_proposal.pdf

[31] **Probing the frontiers of particle physics with tabletop-scale experiments**
D.DeMille and al.
Science, vol. 357, pp. 990–994, 2017
DOI:10.1126/science.aal3003

[32] **Baryon electric dipole moments from strong $\mathcal{CP}$ violation**
FK.Guo, UG.Meißner,
J.High Energ.Phys.2012, 97 (2012)
DOI:10.1007/JHEP12(2012)097

[33] **Measurement of the Permanent Electric Dipole Moment of the Neutron**
C.Abel et al.
Phys.Rev.Lett.124, 081803 (2020)
DOI:10.1103/PhysRevLett.124.081803

[34] **$\mathcal{CP}$ Conservation in the Presence of Pseudoparticles**
R.D.Peccei and H.R.Quinn
Phys.Rev.Lett.38, 1440, (1977)
DOI:10.1103/PhysRevLett.38.1440

[35] **A New Light Boson?**
S.Weinberg
Phys.Rev.Lett.40, 223 (1978)
DOI:10.1103/PhysRevLett.40.223

[36] **Proposal for a Cosmic Axion Spin Precession Experiment (CASPEr)**
D.Budker and al.
Phys. Rev. X 4, 021030 (2014)
DOI:10.1103/PhysRevX.4.021030

[37] **Axionlike dark matter search using the storage ring EDM method**
S.P.Chang et al.
Phys. Rev. D 99, 083002 (2019)
DOI:10.1103/PhysRevD.99.083002

[38] **Axion Dark Matter Detection with Cold Molecules**
P.W.Graham, S.Rajendran
Phys. Rev. D 84, 055013
DOI:10.1103/PhysRevD.84.055013

[39] **Polarization Measurement and Manipulation for Electric Dipole Moment Measurements in Storage Rings**
N.Hempelmann
RWTH Aachen University (2018)
collaborations.fz-juelich.sde/theses/Hempelmann

[40] **Cooler Synchrotron COSY**
R. Maier et al. .
Nuclear Physics A, Vol. 626, Issues 1-2 (1997)
DOI:10.1016/S0375-9474(97)00562-9

[41] **Sources of Polarized Ions** W. Haeberli.
Annual Review of Nuclear Science 17 (1967), pp. 373-426
DOI:10.1146/annurev.ns.17.120167

[42] **Determination of deuteron beam polarizations at COSY**
D. Chiladze et al.
Physical Review Special Topics - Accelerators and Beams 9 (2006).
DOI:10.1103/PhysRevSTAB.9.050101

[43] **Electromagnetic Simulation and Design of a Novel Waveguide RF Wien Filter for Electric Dipole Moment Measurements of Protons and Deuterons**
J.Slim et al.
Nucl. Instrum. Meth. A 828 (2016), pp. 116-124.
DOI:10.1016/j.nima.2016.05.012

[44] **First commissioning results of the waveguide RF Wien filter**
J.Slim for the JEDI collaboration.
Hyperfine Interact. 240.1 (2019)
DOI:10.1007/s10751-018-1547-6

[45] **COSY Prepares the First Measurement of the Deuteron Electric Dipole Moment**
P.Lenisa, F.Rathmann
Nucl. Phys. News 27.3 (2017), pp. 10-13
DOI:110.1080/10619127.2017.1317175

[46] **Spin Coherence Time studies for the storage ring EDM search**
G. Guidoboni
University of Ferrara (2012)
collaborations.fz-juelich.de/theses/Guidoboni

[47] **A new beam polarimeter at COSY to search for electric dipole moments of charged particles**
F.Müller et al.
Journal of Instrumentation, Volume 15 (2020)
DOI:10.1088/1748-0221/15/12/P12005

[48] **Saint-Gobain, LYSO Scintillation Crystal, Cerium doped Lutetium PreLude420 crystal**
Saint-Gobain_LYSO_page

[49] **Epic-Crystal, Ce:LYSO scintillator**
Epic-Crystal_LYSO_page

[50] **Sichuan Tianle Photonics Co., Ltd., LYSO Scintillator Crystal**
Sichuan-Tianle-Photonics_LYSO-page

[51] **Techniques for Nuclear and Particle Physics Experiments : A How-to Approach**,
W.R.Leo
Springer-Verlag, (1994)
doi:10.1007/978-3-642-57920-2e

[52] **Radiation Detection and Measurement, Fourth Edition**.
G.F.Knoll
John Wiley & Sons (2010)

[53] **Atomic weights of the elements. Review 2000 (IUPAC Technical Report)**
J.R.De Laeter et al.
Pure and Applied Chemistry, Vol. 75, No. 6:683-800, 2003.
doi.org/10.1351/pac200375060683

[54] **The NUBASE 2012 evaluation of nuclear properties**
G.Audi et al.
Chinese Physics C, Vol. 36, No.12:1157-1286, 2012.
doi.org/10.1088/1674-1137/36/12/001

[55] **Polarimeter Development for Electric Dipole Moment Measurements in Storage Rings**
F.Müller
RWTH Aachen University (2019)
collaborations.fz-juelich.de/theses/Muller

[56] **US Patent. US 6,624,420 Bl.**
LYSO_patent

[57] **Gamma-Ray Induced Radiation Damage in Large Size LSO and LYSO Crystal Samples**
J. Chen, R. Mao, L. Zhang and R. Zhu
IEEE Transactions on Nuclear Science, vol. 54, no. 4, pp. 1319-1326 (2007)
doi:10.1109/TNS.2007.902370.

[58] **Silicon rubber optical interface EJ-560**
Eljen Technology
Optical_interface_web-page.

[59] **J-SERIES SIPM ARRAY: Silicon Photomultiplier Arrays, J-Series (SiPM),**
ON Semiconductor
MicroFJ-30020-TSV, ARRAYJ-30020-64P-PCB, SensL High Fill-Factor Arrays for Fast Timing Applications
J-SeriesSiPMs.

[60] **Dupon inc. pages**
Teflon. Tedlar. Kapton.

[61] **Development of LYSO detector modules for a charge-particle EDM polarimeter**
D.Shergelashvili et al.
POS 346, (2019)
doi:10.22323/1.346.0145.

[62] **An introduction to the Silicon PhotoMultiplier**
SensL techincal note
SensL_SiPM_note.pdf

[63] **Development of hadron calorimeter modules based onLYSO scintillator crystals**
I. Keshelashvili et al.
Internal Note for JINST submission

[64] **SIS3316-250-14 16 channel 250 MSPS 14-bit**
Struck innovative systeme
SIS3316-250_ADCs

[65] **Silicon Photomultiplier Array PA3315-WB-0808 (15μm pixel) and PA3325-WB-0808 (25μm pixel)**
KETEK GmbH
KETEK_SiPMs.

[66] **Search for electric dipole moments of light ions in storage rings**
F. Rathmann, A. Saleev, and N. N. Nikolaev
Physics of Particles and Nuclei 45,229 (2014)
doi:10.1134/S10637796140108690

[67] **Probing CP violation with the deuteron electric dipole moment**
O. Lebedev, A. Olive, M. Pospelov, and A. Ritz
Phys. Rev. D 70, 016003 (2004)
doi:10.1103/PhysRevD.70.016003

[68] Hamamatsu R1548-07, 24 mm Rectangular dual, Head-on type, Bialkali photocathode (Effective area: 8×18×(2) mm, Spectral response: 300 to 650 nm)
Hamamatsu_PMT_data_sheet

[69] StemLab. Red Pitaya v1.1.
Redpitaya_website

[70] **Development of a multi-channel power supply for silicon photomultipliers reading out inorganic scintillators**
O. Javakhishvili et al. for the JEDI collaboration.
Nuclear Instruments and Methods in Physics Research A (2020)
doi:10.1016/j.nima.2020.164337

[71] **The Lund/LBNL Nuclear Data Search. Decay Properties of ^{176}Lu.**
The_Lund-Lu (1999).

[72] **The Lund/LBNL Nuclear Data Search. Decay Properties of ^{22}Na.**
The_Lund-Na (1999).

[73] **Performance of several solid state photomultipliers with CLYC scintillator**
K. Mesick et al.
IEEE Nuclear Science Symposium and Medical Imaging Conference (2015)
doi: 10.1109/nssmic.2015.7581936

[74] **Test su fascio di un prototipo a GEM finalizzato allo studio del rivelatore centrale dell'esperimento BES III**
N. Canale
Bachelor Thesis (2015)

[75] **Eljen Technology, EJ-200 Bicron plastic scintillator**
`Eljen_Technology,EJ-200_data_sheet`

List of Figures

List of Tables

Acknowledgement

First of all I would like to express my sincere gratitude to Prof. Paolo Lenisa, a supervisor who was always calm and patient in offering his guidance during my PhD journey.

Secondly, I would like to thank Dr. Irakli Keshelashvili, who followed me, guided me, *grilled* me when needed, but also gratified me. A great overlap between a Jedi Master and a Sith one.

I would also like to acknowledge Dr. Joerg Pretz and all the referees that dedicated their time to review my work.

This work would also not have been possible without the precious contribution of Dr. Fabian Müller who preceded me in the research of this detector.

My whole-hearted thanks also go to Andro Kacharava and all the *Georgian team* who were able to make me feel at home whenever I landed in Juelich, where an extraordinary Andrea Pesce was always waiting for providing me any help I needed.

I am extremely grateful to Peppo, Luca and all *SPIN* group who always considered me as one of them from the first day, and to whom I hope to come back one day.

E in questo momento mi permetto di *switchare* all' italiano, per poter esprimere al meglio i miei pensieri e i miei rignraziamenti più sinceri a Giulio, Ila, Riccardo, Marco e tutto il gruppo di πFE, compagni di caffè, pranzi, chiacchere, sfoghi e soprattuto di questo lungo viaggio che mi ha reso l'uomo che sono.

In Rahul ho trovato non solo un compagno di ufficio o di lavoro, ma un amico. Un amico presente anche se spesso in ritardo, capace di ascoltare e replicare sempre con le parole giuste, di instillarmi i dubbi e di sostenermi

nella loro risoluzione, ma il ringraziamento più grande va Vaishnavi che lo sopporta (e che sopporta anche me).

Un pensiero va ai compagni di ADI al fianco dei quali è stato un onore fare attivismo, sperando che i semi che abbiamo piantato crescano forti nelle università.

A tutti i miei amici, vicini e lontani, un **GRAZIE**. Grazie per esserci sempre. La lontananza è nulla quando i cuori sono vicini.

Alla mia famiglia, ai miei genitori, ai miei nonni va la più profonda riconoscenza. Senza la loro presenza e il loro costante supporto sarei perso.

Per ultima, ma sicuramente non per importanza, Rory, che dire? Sei il mio percorso per raggiungere la felicità. In te sono capace di trovare quel posto che chiamo casa ovunque questa sia. Grazie per avermi preso la mano all'inizio della mia università e non averla più lasciata.
Ti amo.

That's all Folks!
So long, and thanks for all the fish!